Center for Photonics and Quantum Materials,
Skolkovo Institute of Science and Technology

Department of Applied Physics,
Aalto University

Hybrid heterojunction solar cells using single-walled carbon nanotubes and amorphous silicon thin films

Pramod Mulbagal Rajanna

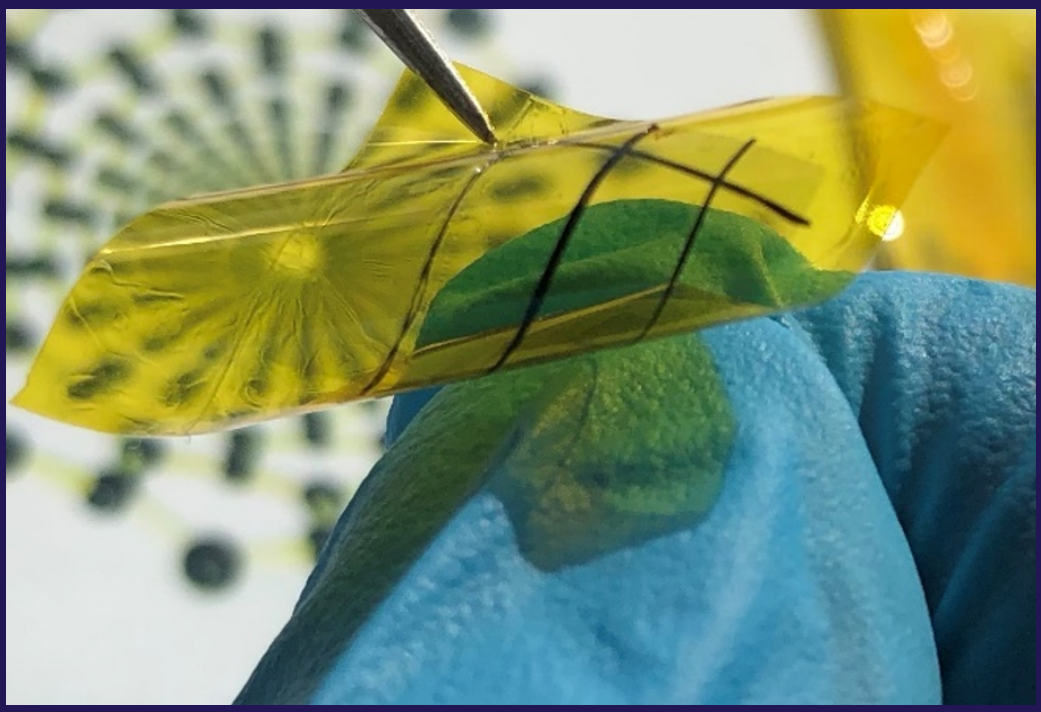

Skoltech
Skolkovo Institute of Science and Technology

Aalto University

DOCTORAL DISSERTATIONS

Skoltech

Skolkovo Institute of Science and Technology

Skolkovo Institute of Science and Technology / Doctoral Program in Physics
DOCTORAL THESIS

Hybrid heterojunction solar cells using single-walled carbon nanotubes and amorphous silicon thin films

Pramod Mulbagal Rajanna

Supervisors:
Professor Albert G. Nasibulin,
Skolkovo Institute of Science and Technology, Russia
Professor Peter D. Lund,
Aalto University, Finland

Defense Jury:
Professor Nikolay A. Gippius (Chairman),
Skolkovo Institute of Science and Technology, Russia
Professor Pavel Troshin,
Skolkovo Institute of Science and Technology, Russia
Professor Dmitry Paraschuk,
Moscow State University, Russia
Professor Aldo di Carlo,
University of Rome, Italy
Professor Anvar Zakhidov,
The University of Texas at Dallas, United States of America

Date & Time: 27 MAY 2020, 17:00 HRS
Venue: ONLINE DEFENSE FROM AALTO UNIVERSITY, FINLAND
(https://aalto.zoom.us/j/63096711658)

Aalto University publication series
DOCTORAL DISSERTATIONS 79/2020

Hybrid heterojunction solar cells using single-walled carbon nanotubes and amorphous silicon thin films

Pramod Mulbagal Rajanna

The public defense on 27th May 2020 at 17:00 (5 p.m.) will be organized via remote technology.

Link: https://aalto.zoom.us/j/63096711658

Zoom Quick Guide: https://www.aalto.fi/en/services/zoom-quick-guide

A doctoral dissertation conducted under a convention for the joint supervision of thesis at Aalto University (Finland) and Skolkovo Institute of Science and Technology (Russia) for the degree of Doctor of Science (Technology) at Aalto University, to be defended, with the permission of the Aalto University School of Science, at a public examination held at the lecture hall N204 of the school on 27th May 2020 at 17:00.

Aalto University
School of Science
Department of Applied Physics
New Energy Technologies

Supervising professors
Professor Peter D. Lund, Aalto University, Finland
Professor Albert G. Nasibulin, Skolkovo Institute of Science and Technology, Russia

Preliminary examiners
Professor Aldo di Carlo, University of Rome "Tor Vergata", Italy
Professor Dmitry Paraschuk, Moscow State University, Russia

Opponent
Professor Anvar Zakhidov, University of Texas at Dallas, United States of America

Aalto University publication series
DOCTORAL DISSERTATIONS 79/2020

ISBN 978-952-60-3892-6 (printed)
ISBN 978-952-60-3893-3 (pdf)
ISSN 1799-4934 (printed)
ISSN 1799-4942 (pdf)
http://urn.fi/URN:ISBN:978-952-60-3893-3

Unigrafia Oy
Helsinki 2020

Finland

NORDIC SWAN ECOLABEL
Printed matter
4041-0619

Aalto University

Abstract

Aalto University, P.O. Box 11000, FI-00076 Aalto www.aalto.fi

Author
Pramod Mulbagal Rajanna

Name of the doctoral dissertation
Hybrid heterojunction solar cells using single-walled carbon nanotubes and amorphous silicon thin films

Publisher School of Science

Unit Department of Applied Physics

Series Aalto University publication series DOCTORAL DISSERTATIONS 79/2020

Field of research Engineering Physics

Manuscript submitted 6 May 2020 **Date of the defence** 27 May 2020

Permission for public defence granted (date) 5 May 2020 **Language** English

☐ **Monograph** ☒ **Article dissertation** ☐ **Essay dissertation**

Abstract

Single-walled carbon nanotubes possess extraordinary optical, electrical, chemical, and mechanical properties. Thin films of randomly oriented SWCNTs have a great potential in many opto-electro-mechanical applications. Moreover, recent developments in photovoltaics have been largely contributed by SWCNTs as a p-type transparent conductor that fulfill the requirements for continuous, fast, and cheap film manufacturing process compatible with the roll-to-roll technology.

The scope of this thesis is the development of a conductive p-type SWCNT transparent conductor and its application in hybrid heterostructure solar cell based on amorphous silicon. For successful implementation of SWCNTs film in solar cells, it is very critical for the SWCNTs to have good physical contact with the material on which it is deposited. At first, quantitative measurements of the adhesion of SWCNT films with substrate materials in air and inert Ar atmosphere using atomic force microscopy was performed. It was found that adhesion of SWCNT films depends on the atmospheric conditions under which it is stored and deposited on a substrate material. The SWCNT film was measured to have higher adhesion in an inert atmosphere. With this understanding, a simple fabrication method of hybrid heterostructure solar cells was proposed in which the SWCNT-PEDOT:PSS composite p-type film forms a coupled continuous hybrid heterojunction with a-Si:H absorber. The optical and electrical properties of this composite was extensively characterized and further optimized by introducing multifunctional components like ultrathin MoO3 and SWCNT fibers. A rationally designed p-type transparent conductor with a combination of SWCNTs-MoO3-PEDOT:PSS-SWCNT fibers composite resulted in a state-of-the-art sheet resistance of 17 Ω/sq at 90% transmittance. Moreover, SWCNT fibers by itself can be used as replacement for traditional metal contacts as demonstrated here. This opens a new avenue in widespread energy technologies, where high hole conductivity and transparency of the material are prerequisites for their successful implementation.

Integrating the developed p-type transparent conductor as a window layer and top electrode on a-Si:H in a nip configuration resulted in a dramatic increase in its power conversion efficiency reaching up to 8.8%. The energy level alignment of these solar cells is carefully engineered at a-Si:H and SWCNTs interface by introducing a ultrathin MoO3 layer that shows the carrier transport by means of band-to-band or trap-assisted tunneling.

Keywords single -walled carbon nanotubes, amorphous silicon, hybrid, heterojunction, thin, films, solar cells.

ISBN (printed) 978-952-60-3892-6 **ISBN (pdf)** 978-952-60-3893-3

ISSN (printed) 1799-4934 **ISSN (pdf)** 1799-4942

Location of publisher Helsinki **Location of printing** Helsinki **Year** 2020

Pages 133 **urn** http://urn.fi/URN:ISBN:978-952-60-3893-3

Acknowledgements

I am deeply indebted to many people for their contributions towards this dissertation, and the quality of my life while working on it.

It has been a privilege to work with Prof. Albert Nasibulin, my supervisor at Skoltech. I am profoundly grateful for his persistent and patient mentoring, support, and friendship through my graduate career, starting from the day he offered me the opportunity to come to Skoltech. I especially appreciate his honest and supportive advice, and his attention to detail while helping me polish my talks and papers. I have learned a lot from my interactions with him, which has helped me to become a more competent researcher.

I am honoured to have worked with Prof. Peter Lund, my supervisor at Aalto University. I thank him for his supervision and examination of this thesis, and for the opportunity to work in his research group (New Energy Technologies). I am deeply grateful for his guidance, continuous support, encouragement, and interest in my work.

I am thankful to Prof. Mikhail Skvortsov, Prof. Alexei Buchachenko, Prof. Nikolay Gippius, and Prof. Pavel Troshin for serving on my committee and for constantly reviewing and evaluating my progress during this thesis.

I am also thankful to Prof. Aldo di Carlo, Prof. Anvar Zakhidov, and Prof. Dmitry Paraschuk for reading this thesis and serving as examiners for my defense.

This dissertation would not have been possible without my collaborators. I thank Dr. Oleg Sergeev and Dr. Hosny Meddeb at DLR institute of networked energy systems, Germany, for working with me on device fabrication and simulation, and Prof. Sergei Bereznev at Tallinn University of Technology for synthesizing organic conductive polymers. I am also thankful for the valuable collaboration with Dr. Olga Volubujeva for SEM, and Dr. Mati Danilson for XPS at Tallinn Unversity of Technology. I would also like to extend my deepest gratitude to Konstantin Larionov and Prof. Pavel Sorokin of National University of Science and Technology MISIS, Moscow, for working with me on adhesion of SWCNT films simulation. I would like to thank Natalia Galochkina, and Natalia Kondrashova for their untiring help during the initial stages of my doctoral thesis with administrative matters.

My doctoral studies have been generously funded by the Ministry of Science and Education, Russian Federation under 'HORIZON 2020' ERA-NET RUS PLUS (RFMEFI61815X0003), the Russian Science Foundation (17-19-01787), a Doctoral Studies Internationalization Program Dora Plus activity 2.2 Fellowship financed by the European Regional Development Fund, an EDUFI Fellowship (# TM-19-11028) from Finnish National Agency for Education, and ASPIRE (Jane and Aatos Erkko foundation, Finland).

Finally, I appreciate the camaraderie and support of my current and former group-mates at Skoltech: Dr. Anastasia Goldt, Dr. Yury Gladush, Dr. Daria Kopylova, Dr. Fedor Fedorov, Dr. Dmitry Krasnikov, Dr. Alexey Tsapenko, Dr. Vsevolod Iakovlev, Dr. Evgenia Gilshteyn, Andrei Starkov (Engineer), Eldar Khabushev, Stepan Romanov, and Alena Alekseeva; and at Aalto: Dr. Imran Ashgar, Dr. Janne Halme, Dr. Kerttu Aitola, Aapo Poskela, and Dr. Lide Yao, without whose help, my work and life would not be smooth. I also sincerely thank Dr. Sergey Luchkin, and Dr. Sergey Tsarev from the Center for Energy Science and Technology, Skoltech for their help, support, and useful discussions during the course of my work. I also extend my deep gratitude to Prof. Tanja Kallio, Aalto University for helping me with ALD depositions.

On a more personal note, I am deeply indebted to my family for the opportunities and support that they provided me. My mother, Prabha and brother, Subodh have been loving and supportive presences, and learned early not to ask when the Ph.D. would be completed. Special thanks to my brother for taking care of the family during my physical absence in their hard times. My father, Rajanna has been an untiring source of sound guidance and advice, which has stood me in good stead. My grandmother, Radha Bai has been a pillar of strength, and has constantly amazed me with her dedication and discipline. Special thanks to my in-laws who have been very supportive and caring.

Finally, I am extremely indebted to my wife Shruthi whose steadfast dedication, help, care, support, and love throughout this journey has continuously amazed me. As I am penning down these words, we have just completed 4 years of our married life. We have blossomed in our relationship from complete strangers to being soul-mates.

My life has been enriched by innumerable people who I cannot begin to thank enough. Saint Tyagaraja's catch-all acknowledgment comes to my rescue:"endarO mahAnubhavulu antarIki vandanamu".

In the memory of my late grand father, Sri Appannachar!!

Espoo, 26 February 2020
Pramod Mulbagal Rajanna

Contents

List of Abbreviations and Symbols

a-Si:H	hydrogenated amorphous silicon
AFM	atomic force microscopy
AF	adhesion force
AR	anti-reflecting
AM	air mass
Al:ZnO	aluminum doped zinc oxide
BE	binding energy
B2BT	band-to-band tunnelling
c-Si	crystalline silicon
CNTs	carbon nanotubes
CO	carbon monoxide
CO_2	carbon dioxide
DOS	density of states
eV	electron-volt
EQE	external quantum efficiency
E_V	valence band edge
E_C	conduction band edge
FOM	figure of merit
FF	fill factor
FWHM	full-width at half maximum
HIT	heterojunction intrinsic thin layer
HSCs	hybrid solar cells
ITO	indium tin oxide
IEC	International Electrotechnical Commission

J_o	reverse saturation current density
J_{SC}	short-circuit current density
KE	kinetic energy
KPFM	kelvin probe force microscopy
MPP	maximum power point
MoO_3	molybdenum trioxide
MEH-PPV	Poly[2-methoxy-5-(2-ethylhexyloxy)-1,4-phenylene-vinylene]
N(E)	density of states
NIR	near infrared
NWs	nanowires
η	power conversion efficiency (PCE)
n	diode ideality factor
OCPs	organic conductive polymers
PV	photovoltaics
PCE	power conversion efficiency
PECVD	plasma enhanced chemical vapor deposition
PEDOT:PSS	poly(3,4-ethylenedioxythiophene) polystyrene sulfonate
P3HT	Poly(3-hexylthiophene)
PCBM	Phenyl-C61-butyric acid methyl ester
PCPTDBT	Poly[2,6-(4,4-bis-(2-ethylhexyl)-4H-cyclopenta [2,1-b;3,4-b′]dithiophene)-alt-4,7(2,1,3-benzothiadiazole)]
PMMA	Poly(methyl methacrylate)
PI	polyimide
PDMS	polydimethylsiloxane
R_{sh}	sheet resistance
R_S / R_{sr}	series resistance
R_{Sh} / R_p	shunt resistance
RH	relative humidity
RMS	root mean square
R	radius of curvature
SWCNTs	single-walled carbon nanotubes

SWE	Staebler-Wronski-Effect
SiO_2	silicon dioxide
SAFD	surface adhesion force density
SEM	scanning electron microscopy
TCF	transparent conductive film
TEM	transmission electron microscopy
TAT	trap-assisted tunnelling
UV	ultraviolet
Vis	visible
V_{OC}	open-circuit voltage
V_{bi}	built-in voltage
W_f	work-function
XPS	X-ray photoelectron spectroscopy

List of Chemicals and Elements

Au	gold
Ag	silver
Al	aluminum
Ar	argon
Cu	copper
$HAuCl_4$	chloroauric acid
HF	hydrofluoric acid
IPA	isopropanol
KOH	potassium hydroxide
Pt	platinum
ZrO_2	zirconium oxide

List of Publications

This doctoral dissertation consists of a summary of the following publications which are referred to in the text by their numerals

1. Pramod M. Rajanna, Sergey Luchkin, Konstantin V. Larionov, Artem Grebenko, Zakhar I. Popov, Pavel B. Sorokin, Mati Danilson, Sergei Bereznev, Peter D. Lund, and Albert G. Nasibulin. Adhesion of Single-Walled Carbon Nanotube Thin Films with Different Materials. *J. Phys. Chem. Lett. 2020, 11, 504−509.*

2. Pramod M Rajanna, Evgenia P Gilshteyn, Timur Yagafarov, Alena K Aleekseeva, Anton S Anisimov, Alex Neumüller, Oleg Sergeev, Sergei Bereznev, Jelena Maricheva, and Albert G Nasibulin. Enhanced efficiency of hybrid amorphous silicon solar cells based on single-walled carbon nanotubes and polymer composite thin film. *Nanotechnology 29 (2018) 105404 (10 pp).*

3. Alena K. Alekseeva, **Pramod Mulbagal Rajanna**, Anton S. Anisimov, Oleg Sergeev, Sergei Bereznev, and Albert G. Nasibulin. Synergistic Effect of Single-Walled Carbon Nanotubes and PEDOT:PSS in Thin Film Amorphous Silicon Hybrid Solar Cell. *Phys. Status Solidi B 2018, 255, 1700557.*

4. Pramod M. Rajanna, Hosni Meddeb, Oleg Sergeev, Alexey P. Tsapenko, Sergei Bereznev, Martin Vehse, Olga Volobujeva, Mati Danilson, Peter D. Lund, Albert G. Nasibulin. Rational design of highly efficient flexible and transparent p-type composite electrode based on single-walled carbon nanotubes. *Nano Energy 67 (2020) 104183.*

5. Pramod M. Rajanna, Peter D. Lund, Albert G. Nasibulin. Hybrid heterojunction solar cells based on single-walled carbon nanotubes and amorphous silicon thin film-a mini review. S*ubmitted, May 2020.*

Author's Contribution

Publication 1: Adhesion of Single-Walled Carbon Nanotube Thin Films with Different Materials.

The author is mainly responsible for this work. The author developed the idea, designed & conducted the experiments and measurements, and analysed the data. The author was responsible for writing the manuscript, communicating with the journal editor and answering to the reviewers' queries.

Publication 2: Enhanced efficiency of hybrid amorphous silicon solar cells based on single-walled carbon nanotubes and polymer composite thin film.

The author is mainly responsible for this work. The author designed & conducted the experiments, fabricated & measured the devices, and analysed the data. The author was responsible for writing the manuscript, communicating with the journal editor, and answering to the reviewers' questions.

Publication 3: Synergistic Effect of Single-Walled Carbon Nanotubes and PEDOT:PSS in Thin Film Amorphous Silicon Hybrid Solar Cell.

The author is mainly responsible for conceptualization of the idea, design of experiments, measurements, data analysis, and jointly writing the paper. The author was responsible for answering to the reviewers' questions.

Publication 4: Rational design of highly efficient flexible and transparent p-type composite electrode based on single-walled carbon nanotubes.

The author is mainly responsible for this work. The author designed & conducted the experiments, fabricated & measured the devices, and analysed the data. The author was responsible for writing the manuscript, and answering to the reviewers' questions.

Publication 5: Review: Hybrid heterojunction solar cells based on single-walled carbon nanotube and amorphous silicon thin films.

The author is mainly responsible for this work and writing the paper.

1. Introduction

The growing world population with its urbanization are increasing energy consumption [1,2], which is projected to double by 2050 and triple by 2100 [3]. Currently, most of the energy is still supplied by fossil fuels, which has led to severe environmental problems [3], notably climate change. Renewable energy technologies offer solutions to this problem and are expected to be the fastest-growing energy technologies in the coming years, with an expected average growth of 2.3% per year till 2040 [4]. Among renewable energy technologies, photovoltaics (PV) has seen a sharp growth in the last decade with a current generational capacity of 510 GW_p [5]. This is a result of achieving 'grid-parity' in most countries and decreased solar cell costs of over 85% between end of 2009 and first half of 2018 with a total investment of more than $142 billion [6]. The establishment of grid-parity will further accelerate PV installations allowing it to become a leading contributor to world electricity production by 2040 [7].

Among PV devices, crystalline silicon (c-Si) solar cells have dominated the market with power conversion efficiencies (PCEs) exceeding 26% thanks to their heterojunction with intrinsic layer technology based on thin hydrogenated amorphous silicon (a-Si:H) passivating layers and on interdigitated back contacts on n-type silicon wafers [8,9]. However, as recent technologies are evolving into flexible, versatile and portable electronics, there is also demand for manufacturing solar cells in roll-to-roll processes. Such solar cells would be thin, flexible and could be directly incorporated into buildings, e.g. as roofing shingles. Thin film solar cells, including those made of a-Si:H are suitable materials for roll-to-roll production with the advantages of reduced fabrication costs, increased light absorptivity, and reduced solar cell thickness, thereby reducing material consumption and device weight [10]. Additionally, a-Si:H can be deposited on any foreign substrate by plasma enhanced chemical vapor deposition (PECVD) at close to room temperature [10]. However, as the carrier mobility of a-Si:H is low, an expensive transparent conducting layer as the top contact is needed, such as indium tin oxide (ITO) [11]. Therefore, ITO-free solar cells have become an important focus of research for next generation PV devices

[12,13,22,23,14–21]. Several studies have been reported combining inorganic Si, a-Si:H with organic conductive polymers (OCPs) [12,13,16,19,22,24]. Moreover, carbon-based materials such as carbon nanotubes (CNTs), in particular single-walled CNTs (SWCNTs), have made major contributions to solar cell development in recent years [25–29] and are termed as 'hybrid solar cells (HSCs)'. Although, several attempts have been made to develop HSCs as a-Si/CNTs, a-Si/OCPs, and CNTs/OCPs, their PCEs have been too low for practical applications [16,30–32].

CNTs are promising materials for thin-film solar cells owing to a wide range of properties from conductors to semiconductors with variable bandgaps based on their atomic structure [33]. While CNTs can have multiple number of walls, SWCNTs exhibit excellent opto-electrical advantages over double and multi-walled CNTs [34]. For this reason, SWCNTs have been used extensively as electrodes in many solar cell devices, replacing brittle ITO, fluorine-doped tin oxide and expensive metal electrodes, especially in c-Si, polymer and more recently in perovskite-based solar cells [25,26]. Although SWCNTs have superior opto-electro-mechanical properties, solar cells based on SWCNTs have not yet matured for practical applications. Moreover, our understanding of the limitations of SWCNTs and solutions to optimize these for PV applications is limited.

This doctoral thesis therefore aims to investigate the underlying fundamental limitations of SWCNTs and provide necessary innovative solutions to allow their optimal usage in PV and other opto-electronic applications. The mechanisms affecting SWCNTs/a-Si:H heterostructures like physical contact or adhesion of SWCNTs with a-Si:H, the opto-electrical properties and inter-tube resistance of SWCNTs, and carrier transport and collection at the interface of a-Si:H and SWCNTs are studied. An energy efficient, environmentally friendly and low cost process technology is developed for fabrication of hybrid thin film solar cells combining a-Si:H and SWCNT films by eliminating boron-doped a-Si:H, transparent conductive layers like ITO, and other traditional metal layers like Au, Ag, Al, and Cu. SWCNTs are proposed as a window layer p-type transparent conductive film (TCF), a potential replacement for all the aforementioned layers and processes, thereby resulting in a less energy-consuming process technology, minimizing material consumption and reducing the net cost.

Despite the relatively short time for development of HSCs based on a-Si:H and SWCNT films the results achieved in this project were motivating. However, their relevant working principles have scarcely been investigated or

are limited to SWCNTs as an electrode. The excellent conductivity and transparency make the SWCNTs material an excellent choice for this task. It has high conductivity with semi-metallic characteristics and is doped to its p-type state. The main highlights of this thesis are the first quantitative evaluation of the adhesion of SWCNT films to some common substrates, development of a rational design for a state-of-the-art p-type TCF using multifunctional component layers to form a single composite layer based on SWCNTs and the establishment of a-Si:H/SWCNTs HSC design with a state-of-the-art PCE of 8.8%.

This thesis is based on the five original publications listed in the List of Publications and divided into five chapters. It is organized as follows: Chapter 1 gives an overview as well as the outline of the thesis. Chapter 2 comprises the brief background of HSCs as well as materials used in this thesis as thin films of a-Si:H, SWCNTs, PEDOT:PSS, molybdenum oxide, and CNT fibers. A short review of a-Si:H and SWCNT HSCs is given. Chapter 3 presents details of the experimental methods for optical and electrical measurements, chemical composition, surface morphology, and solar cell characterization. Chapter 4 presents the main results on the influence of adhesion of SWCNT films to common substrates, introduction of PEDOT:PSS into SWCNT films and its opto-electrical properties, HSC fabrication and characterization, a rational design of a TCF using a combination of SWCNT film, transition metal oxide, PEDOT:PSS and SWCNT fibers carefully matched to form a state-of-the-art p-type TCF, opto-electro-mechanical properties of p-type TCF, fabrication of HSCs based on a-Si:H and TCF, and characterization of HSCs. Chapter 5 summarizes this thesis.

2. Hybrid solar cells and their components

"Hybrid" solar cells combine inorganic and organic materials that are matched for desired physical and opto-electrical properties, functionalization of surfaces or organic/inorganic heterostructures [35]. Device performance is heavily influenced by their electronic structure [35]. The approach in this work is to combine a-Si:H and SWCNT with PEDOT:PSS thin films as a highly efficient hybrid heterostructure solar cell. As SWCNT films are predominantly p-type, they are combined with hole transport PEDOT:PSS as a composite to form p-type TCFs. The current is mainly generated in the a-Si:H absorber layer. Furthermore, these hybrid solar cells are manufactured using a simple fabrication process that is detailed in this thesis.

2.1 Previous work and development

During the last decade, the development of HSCs utilizing thin-film a-Si:H, SWCNTs and OCPs like PEDOT:PSS, P3HT, PCBM, MEH-PPV, PCPDTBT and polypyrole has gained increasing interest thanks to their low fabrication cost, large area and the ability to produce mechanically flexible photovoltaic devices at a low processing temperature [12,13,16,17,19,36]. A large body of work has reported a-Si:H/OCPs with PCEs up to 3%. Further, carbon nanomaterials and especially SWCNTs have also been employed owing to their exceptional properties forming heterostructure solar cells with OCPs and a-Si:H, respectively [30–32,37–39]. SWCNTs have also made a major contribution to heterostructure solar cell development with C-Si and more recently with perovskites [26,29].

However, significant progress and the breakthroughs required for the use of CNTs/OCPs and CNTs/a-Si:Hs in real applications have not been achieved. Some reasons for this include the poor opto-electronic properties of SWCNTs, highly unstable OCPs, non-conformity and poor physical contact, large interface resistance, a high Schottky barrier causing band-offsets, and the high tube-tube resistance of SWCNTs. These issues have led to very modest device performance with low currents and high junction recombination [26,40].

There is hence significant potential for the improvement of these materials to allow them to be contenders for flexible and wearable electronic applications. In this work, each of the problems is systematically studied to provide solutions to overcome the limitation of HSC efficiency. The material combines abundance and high transparency with good electrical properties and non-destructive techniques are used for its fabrication.

2.2. Amorphous Thin-Film Silicon

Thin-film a-Si is a well-studied material that has long range disorder and can be deposited by silane as a precursor gas in a CVD process. In this form, however a-Si has a high defect density (10^{19} cm^{-3}) of dangling bonds. They act as primary recombinations centers that reduce the carrier lifetime, diffusion and drift lengths, and pin the Fermi energy such that the material cannot be effectively n- or p-type doped, and hence is not electronically useful. However, it was shown that incorporation of about 10% hydrogen during the deposition process greatly reduces the density of these defects to about 10^{15} cm^{-3}, and that this hydrogenated material can be either n- or p-type doped [41]. The a-Si:H has a larger mobility gap and optical absorption coefficient than c-Si. Unlike c-Si, the edges of the valence and conduction bands are not well defined, and exhibit a continuous distribution of density of states. The energy states in which the charge carriers can be considered as free carriers are described by wave functions that extend over the whole atomic structure. These states are nonlocalized and are called extended states. The disorder in a-Si:H causes the wave functions of the tail and defect states to become localized within the atomic network. These states are called localized states. Consequently, mobility that characterizes the transport of carriers through the localized states is strongly reduced. This feature of a sharp drop in the mobility of carriers in the localized states in comparison to the extended states is used to define the bandgap in a-Si:H. This bandgap is denoted by the term mobility gap, E_{mob}, because the presence of a considerable density of states in the mobility gap is in conflict with the classical concept of a bandgap without any allowed energy states. The energy levels that separate the extended states from the localized states in a-Si:H are called the valence band, E_V, and the conduction band, E_C, mobility edges. This is shown in Figure 2-1 [11,42]. The mobility gap of a-Si:H is larger than the bandgap of single crystal silicon and has a typical value between 1.7 eV and 1.8 eV [11]. Therefore, just 1 μm thickness of a-Si:H is sufficient to absorb virtually all of the incident light that is ≥mobility gap [11].

Hence, a-Si:H has played a crucial role in solar cells as intrinsic absorber layers with doped layers for building PIN and NIP junctions, and an increasingly important role in combination with c-Si in HIT solar cells [11,41,43]. The advancement of thin-film electronics and in particular solar cells has been credited largely to a-Si:H. It has the distinct advantage of cost-effective deposition from the gas phase by PECVD at relatively low temperatures (<100 °C), thereby enabling its deposition onto temperature-sensitive and low cost substrates such as polymers [44]. Besides a variety of designs of the plasma reactor (diode, triode configurations), a range of frequencies from radio frequencies to ultrahigh frequencies is applied. Modifications like remote plasma reactors, where dissociation is spatially separated from deposition, or dissociation by an electron cyclotron resonance reactor or a hot wire CVD, have an influence on film quality. More detailed information on the material and its processes can be found in the literature [11,41,44].

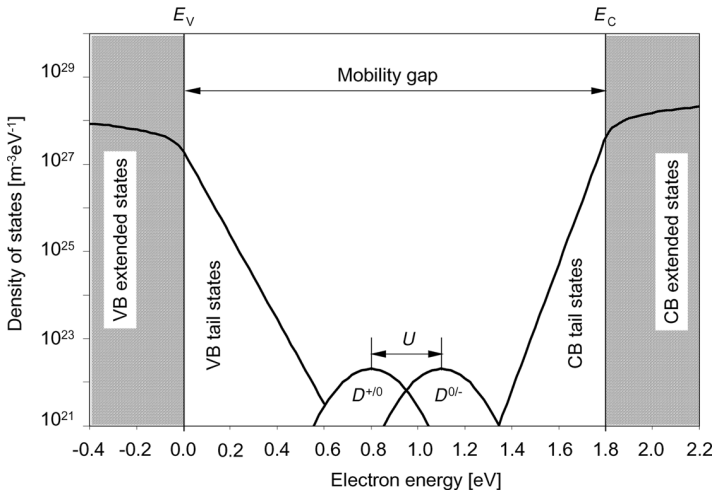

Figure 2-1. Electronic structure in amorphous silicon described by the density of states as function of energy N(E) [11,42].

In general, three types of states can be identified: (1) extended band-like states (shaded grey area in Figure 2-1), similar to the conduction and valence band in c-Si, resulting from overlapping electronic wavefunctions of non- or only slightly distorted bonds in the network. Charge carriers can move freely in these states [45]. (2) Localized band-like states or tail states, resulting from more strongly distorted and thus weak bonds, where no overlap of wavefunctions occurs. At room temperature, charge carriers in these states are frequently excited to the conduction band and recaptured, resulting in a reduced mobility. Consequently, mobility edges are defined at the transition from localized to extended states, as indicated in Figure 2-1. In between the mobility

edges, the mobility gap serves as an equivalent to the band gap in crystalline silicon. As the edge from extended to localized states is not abrupt, the value for the mobility gap depends on its definition or evaluation, impeding a direct comparison of absolute values. (3) Localized defect states resulting from highly distorted or mostly non-saturated bonds, so-called dangling bonds. These build up a distribution of defect states inside the band gap, which act as recombination centres for charge carriers and thus reduce the lifetime of excess carriers [41,45].

The a-Si:H stability was examined by Staebler and Wronski in 1977, who deduced that the conductivity of a-Si:H films is reduced upon illumination [46]. This so-called Staebler-Wronski effect (SWE) is due to an increased defect density resulting from broken Si-H bonds under sample illumination [47]. This in turn results in a deterioration of solar cell performance, which stabilizes after a certain illumination time. The effect is metastable and initial efficiencies of solar cells can nearly be retrieved upon annealing at temperatures below the deposition temperature, typically at 160 ◦C for deposition temperatures of 180-200 °C [11].

2.3 SWCNT films

SWCNTs have rapidly been incorporated into the development of new types of solar cells comprising SWCNT films, graphene or a polymer and silicon or more recently perovskites [25,26,28,29]. They have the advantages of a simple structure and fabrication, low-cost and promising performance.

SWCNTs are hollow cylinders that can be visualized as having been formed by rolling-up a graphene sheet which is an extended planar hexagonal lattice of purely sp^2-bonded carbons [48]. This unique structure has high flexibility, surface area, carrier mobility, chemical stability and optoelectronic properties. Owing to its direct sub-band gaps, tunable photoabsorption from the NIR to the UV range and high conductivity, thin SWCNT films can be used not only as perfect p-type window layers to collect holes in solar cells, but also as transparent conductive electrodes [26,40]. Among SWCNT production techniques, thin films produced by aerosol CVD have been the most successful in heterojunction solar cells [25]. In this section, SWCNT films produced by the aerosol CVD technique are briefly discussed. More information on the material and its processes can be found in the literature [25,33,48].

Aerosol CVD synthesis. Among the various synthesis approaches, the aerosol CVD (floating catalyst) method has proven to be a reliable technique

to produce high-quality SWCNT films with tunable parameters. The main advantages of this method are the high purity and uniformity of the product, a high-yield process completely free from liquid phase or surfactant cleaning, reduced bundle formation and flexibility in terms of substrate selection. All the SWCNTs film used in this thesis were synthesized by the aerosol (floating catalyst) method and consist of 1/3 metallic and 2/3 semiconducting nanotubes; therefore they have a certain bandgap and chirality, that influences its electrical and optical properties [49]. The statistical fractioning of randomly oriented SWCNTs in films limits the conductivity by the introduction of Schottky barriers between the nanotube contacts, which leads to contact resistance that cannot be overcome without further modification process [49].

Briefly, the synthesis is based on catalyst thermal decomposition and a CO disproportionation reaction on a catalyst particle surface. During this process, catalyst particle formation and subsequent SWCNT growth take place directly in the reactor flow (Figure 2-2a). The reactor consists of a quartz tube placed in a furnace (hot zone), a precursor cartridge (filled with ferrocene/silicon dioxide mixture) and a gas supply system (Figure 2-2a). Catalyst precursor (ferrocene) vapor is delivered into the reactor hot zone by passing a gas stream (CO) through the pre-heated cartridge at 60 °C. Additionally, the flow of CO and CO_2 mixture passes through the reactor. Here, CO_2 increases the catalyst lifetime as it preserves the catalyst from deactivation [50,51]. The addition of CO_2 helps to control the output parameters of produced SWCNTs (for instance, longer nanotubes can be yielded at long catalyst lifetimes) as well as other synthesis conditions. The typical synthesis temperature range is from 750 to 1100 °C. Therefore, after partial ferrocene decomposition and catalyst particle formation in the hot zone, catalytic CO disproportionation takes place along with the decomposition of hydrocarbon and ferrocene, which eventually lead to the dissolution of carbon into nanoparticles. This results in nanoparticles saturation by carbon and carbon layer formation on the catalyst particle surface (SWCNTs are formed in cases when catalyst particle size is less than or equal to 5 nm). The SWCNTs film is then collected on a nitrocellulose filter. The surface morphology of randomly oriented SWCNTs is shown in Figure 2-2b and c.

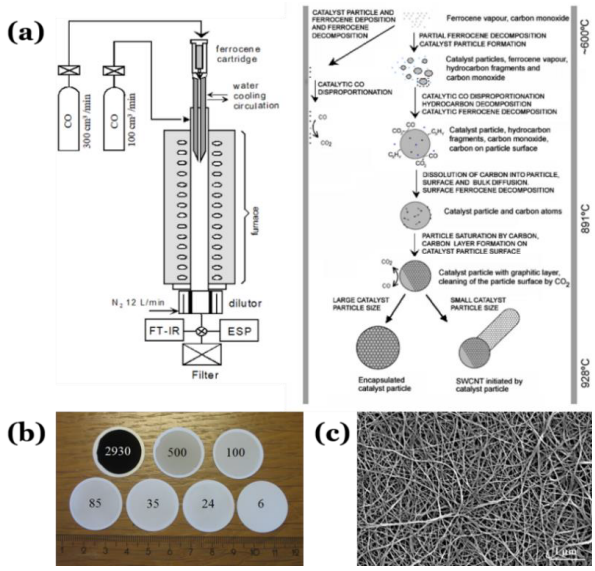

Figure 2-2. (a) Typical SWCNT aerosol-synthesis reactor (left) and SWCNT formation scheme during the synthesis process (right) [49,51,52]; **(b)** SWCNT films collected on nitrocellulose filters with different thicknesses [53]; **(c)** Surface morphology of randomly oriented SWCNTs.

Doping: SWCNT films reveal various outstanding optical and electronic properties but still have an issue with the reduction of Schottky barrier between semiconducting and metallic nanotubes. This has led to several processing methods to increase their optoelectronic characteristics. The techniques are based on the shift of the Fermi level (E_F for metallic (M) or semiconducting (S) nanotubes) position. In pristine nanotubes the E_F is usually located in the middle of density of states (DOS). Therefore, if the electrons or holes are added to SWCNTs, the E_F is shifted upward (n-type doping) or downward (p-type doping), compared to the initial position (Figure 2-3a and b), and conductivity increases. Normally, due to the presence of oxygen in the atmosphere, nanotubes become p-type doped, which is again related to the shift of E_F under ambient conditions.

Among several key strategies to modify the charge carrier type (substitutional doping, doping in an electrostatic field, work function change ($\Delta\Phi$) when connected to the metal, ambipolarity, etc.), the adsorption doping has numerous advantages [54,55]. The feasibility reason for this method is the exposure of all carbon atoms of SWCNTs to the environment. In this way, any atom/molecule put on a SWCNT causes charge transfer between the atom/molecule and a nanotube [56,57]. Thus, the selection of an appropriate chemical

dopant that will be put on the SWCNTs is highly important to achieve the desired conductivity. Chloroauric acid ($HAuCl_4$) and gold chloride ($AuCl_3$) are the chemical dopants used in this study as reported [54,56].

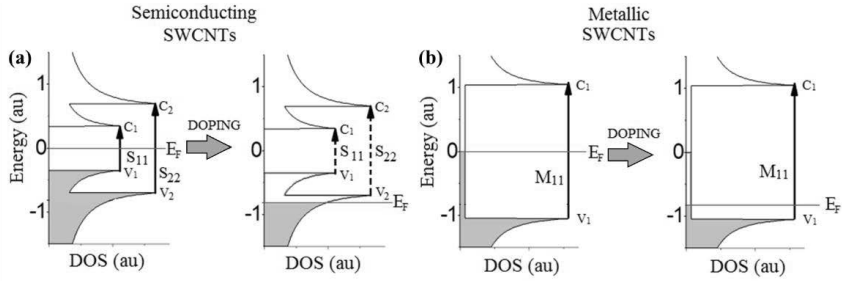

Figure 2-3. Density of states (DOS) of pristine and doped **(a)** semiconducting; and **(b)** metallic SWCNTs, respectively.

2.4. PEDOT:PSS

PEDOT:PSS (Figure 2-4), one of the most classic OCPs, is the most widely used material for fabricating existing PVs as hole transport layers, displays and transistors and various sensing electronics including strain, pressure-, temperature-, humid-, and biosensors, because of its optical transparency in the visible range, tunable electrical conductivity and W_f, high flexibility, stretchability, etc. [58]. PEDOT:PSS is a polymer electrolyte incorporating conducting conjugated PEDOT with positive charges and insulating PSS with negative charges. Oxidized PEDOT is highly conductive, but is insoluble in water; whereas insulating PSS facilitates the dispersion of PEDOT in water and enables a stabilized PEDOT configuration by Columbic attractions. As-cast PEDOT:PSS films have an inherent direct current electrical conductivity (σ) of no more than 1.0 S cm^{-1}; whereas the modified films are able to show a substantial improvement in conductivity to 2–3 orders of magnitude (the best values reach 4000 S cm^{-1}) through the modification of polar solvents, strong acids, and ionic liquids [59]. Additionally, the films have a typical W_f: 4.8–5.4 eV that is favored for charge transfer and injection with fast kinetics, and the films are preferably used in opto-electronic devices as a p-type contact layer [58]. In this study, PEDOT:PSS was used from the pre-mix of commercially available 5 ml PEDOT:PSS (1.3 wt.%; Sigma-Aldrich) aqueous suspension with 120 µl of glycerin, 250µl of N-methylpyrrolidone, and 6.25 ml of isopropyl alcohol (IPA).

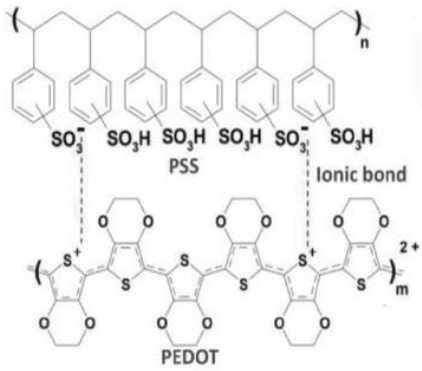

Figure 2-4. Chemical structures and features of PEDOT:PSS [59].

2.5 Molybdenum oxide

The use of metal oxide layers such as MoO_3 in solar cells has recently been in focus [29,60–62]. In the past few years, the high work-function of MoO_3 (6.5 to 6.8 eV) commonly deposited by thermal evaporation, sputtering, and atomic layer deposition has been successfully used as a hole-injection and –extraction material in solar cells which creates a large built-in voltage[18,61–64]. Park *et al.* replaced the conventional p-type a-Si:H and hydrogenated amorphous silicon carbide with MoO_3 [60]. In a recent report, a c-Si solar cell with a MoO_3 layer between a SWCNT film and Au anode was fabricated [29]. The PCE increased to 14.2% with the MoO_3 layer compared to 11.5% for the pristine SWCNTs/Si solar cell with a reduced reflection, indicating AR properties of MoO_3 [29]. Recently MoO_3 nanoparticles have been incorporated into PEDOT:PSS solution to form a composite which is an efficient hole transport layer in perovskite solar cells [65].

2.6 CNT fibers

In traditional p-n or p-i-n junction solar cell structures, either fine metal grids with Au, Ag, Al, Cu, or Ag NWs are deposited, or sputtered ITO as a transparent conductive oxide film is used [66]. However, when using a SWCNT film, which is a randomly oriented porous network of interconnected nanotubes, it is possible that metals will penetrate through the porous network and get into contact with the active layers underneath to form undesired metal-semiconductor junctions during deposition. Jeong *et al.* deposited gold grids on PEDOT:PSS/Si solar cells which resulted in a reduced current density (J_{sc}) from 35.6 to 31.0 mA/cm² [67]. To overcome this problem, Li *et al.* used a high density and low porous network of SWCNT films in their SWCNT/C-Si solar cell with spin-coating of Ag NWs [66]. In a recent report, CNT strips have been used

on top of transparent CNT films to fabricate a heterojunction CNT/Si solar cell. The authors showed that the CNT strips not only decrease the series resistance of the CNT thin film, but they also helped to form a better junction with the underlying Si resulting in an improved PCE [28].

3. Methods

This section details the basics of all the experimental measurement techniques used in this work: the optical properties of SWCNT films, PEDOT:PSS, SWCNTs-PEDOT:PSS composite, and SWCNT fibers were measured using UV-Vis-NIR spectroscopy; the chemical composition of the SWCNT film, MoO_3 and depth profile of HSC were measured using XPS; the electrical properties of SWCNT films, PEDOT:PSS, SWCNTs-PEDOT:PSS composite, and SWCNT fibers were measured using the linear 4-probe method; the structural analysis and surface morphology of the SWCNT films and the SWCNT-PEDOT:PSS composite were measured using TEM and SEM, and the cross-section of HSC was also measured using SEM; the surface morphology, RMS roughness and surface potential for work-function of the SWCNT films and the SWCNT-PEDOT:PSS were measured using AFM and KPFM; and all the fabricated HSCs were measured for their performance using J-V and EQE measurements.

3.1 UV-Vis-NIR spectroscopy

UV-Vis-NIR spectroscopy is a common and robust technique to study the optical properties of SWCNTs when used as TCFs that depend on the transmittance value at 550 nm (T_{550}). In addition to that, the film thickness can be easily estimated when the absorbance is known as following: Thickness (nm) = 417 × $Absorbance_{550\ nm}$ [68]. The typical set-up consists of a white light source, diffraction mirrors enabling wavelength selection and detectors, covering the studied wavelength range. In **Publication 1**, the absorbance was recorded by a Perkin-Elmer Lambda 1050 spectrometer with a wavelength ranging from 175 to 3200 nm, the aerosol synthesized SWCNT thin film is dry-transferred [53] onto optically transparent quartz (20×25×1 mm). In **Publication 3**, optical transmittance was recorded by a Perkin-Elmer Lambda 1050 spectrometer with a wavelength ranging from 175 to 3200 nm, total reflectance was measured using a Bentham PVE 300 (300-800 nm). Both the equipment were first calibrated without samples and reference. After calibration the measurements were conducted by placing the sample in the beamline center and using a bare

quartz substrate as a reference. In **Publication 4**, total transmittance was recorded using a Bentham PVE 300 (300-800 nm).

3.2 XPS measurements

XPS is a surface analysis technique which provides both elemental and chemical state information virtually without restriction on the type of material analyzed. The sample is illuminated with X-rays - monochromatic or unfiltered Al Kα or Mg Kα - and photoelectrons are emitted from the surface. The kinetic energy of these emitted electrons is characteristic of the element from which the photoelectron originated. The position and intensity of the peaks in an energy spectrum provide the desired chemical state and quantitative information [69]. The chemical state of an atom alters the BE of a photoelectron which results in a change in the measured KE. The BE is related to the measured photoelectron KE by the simple equation; BE=hv-KE, where hv is the photon (x-ray) energy. The chemical or bonding information of the element is derived from these chemical shifts [69].

In **Publications 1, 3 and 4**, a Kratos Analytical Axis Ultra DLD spectrometer equipped with a monochromatic Al Kα X-ray source and an achromatic Mg Kα / Al Kα dual anode X-ray source was used to measure the elemental composition of ZrO2 and a-Si:H cantilever tips, SWCNT film, and MoO3, respectively. The monochromatic Al Kα anode (1486.6 eV) was operated at 150 W and 15 kV. The 180° hemispherical energy analyzer with an average radius of 165 mm was operated using a hybrid lens mode at a pass energy of 160 eV for survey spectra and 20 eV for regions spectra. Additionally, in **Publication 4**, 40 eV pass energy was used for depth profile of the TCF3 hybrid solar cell. XPS spectra were recorded at a takeoff angle of 90° from the surface of the sample holder using an aperture slot of 300 × 700 μm2. Samples were mounted on a stainless-steel sample bar (130 × 15 mm2). The binding energy values were calculated on the basis of the C 1s peak at 284.6 eV. The relative atomic concentrations of the elements were determined from the appropriate integrated peak areas at the core level and the sensitivity factors provided by the original analysis Kratos Vision 2.2.10 software. The Shirley background subtraction was used to calculate relative atomic concentrations. For surface cleaning and the bulk composition information, Minibeam I ion (Ar+) source (2 keV, 10 mA, 30 s per cycle) was used.

3.3 Four-point probe measurement

The most common method for measuring the sheet resistance of any semiconductor material is the 4-point probe. It is well-known that for a regular three-dimensional conductor, the resistance R follows [70]

$$R = \rho\frac{L}{A} = \rho\frac{L}{W \cdot t} = \frac{\rho}{t} \cdot \frac{L}{W} = R_S \cdot \frac{L}{W}$$

where ρ is the resistivity, L is the length, A is the cross-section, W is the width and t is the thickness of thin film.

For the 4-point probe, the linear method is used throughout this thesis (Jandel RM3000), the sheet resistance, R_s and corresponding conductivity, σ is evaluated in the following way:

$$R_S = \frac{\rho}{t} = \frac{\pi}{\ln 2} \cdot \frac{V_{probe}}{I_{probe}}\ \Omega/\square \ and\ \sigma = \frac{1}{\rho}\ S/cm.$$

The idea of the linear 4-point probe is to use four electrodes, which are linearly placed close to each other and far from the sample edges as shown in Figure 3-1. Two electrodes are used to apply current (outer electrodes), while the other two register the voltage (inner electrodes). The separation of current and voltage electrodes eliminates the lead and contact resistance from the measurement. Since the measured resistance of the film depends on its thickness, usually two more characteristics are calculated, which can be used to compare different materials – the FoM and equivalent sheet resistance (R_{90}) for a film with R_S and light absorbance at 550 nm (A_{550}) [53]:

$$FoM = \frac{1}{R_S \cdot A_{550}};\ R_{90} = \frac{R_S \cdot A_{550}}{\log(10/9)}.$$

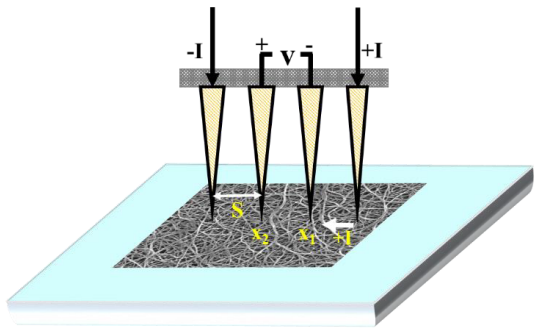

Figure 3-1. Schematic of 4-point probe measurement [70].

3.4 SEM and TEM

Electron microscopy techniques are powerful tools for the characterization of individual SWCNTs as well as the film morphology. In this work, we used SEM to observe the surface morphology and cross-section of the SWCNT film and hybrid solar cells; and TEM to analyze the nanoscale structure of SWCNT film.

In **Publication 1**, the SEM measurements were performed using a JEOL JIB-4700F Multi Beam system for the surface morphology and cross-section of the SWCNT film. Prior to ion milling, a 1 μm thick Pt layer was deposited to avoid gallium ion beam damage to the nanotube film. For coarse and fine milling, the probe currents were set to 3 nA and 300 pA at 30 kV, respectively. The final polishing was performed by a 30 pA probe current and 5 kV accelerating voltage. In **Publication 2**, a Carl Zeiss NEON 40 EsB field emission SEM combining a GEMINI lens design with an advanced Canion FIB column (equipped with Gallium liquid metal ion source) was used (installed at DLR Institute of Networked Energy Systems, Oldenburg, Germany) for measuring the cross-section of the hybrid solar cell. Prior to investigation, the sample was coated with a thin metal contrast layer. The cross-section was formed with focused ion beam at 2 mA emission current, 30 kV acceleration voltage and 10 nA milling current. Multi-step polishing was performed at milling currents from 200 to 20 pA. The SEM image was obtained at 20 kV acceleration voltage using in-lens secondary electron detectors. In **Publication 3,** a FEI Helios Nanolab 660 SEM was used with a maximum accelerating voltage of 30 kV to investigate the morphology of SWCNT film and SWCNT/a-Si solar cell cross-section. In **Publication 4,** surface morphology and film thickness were measured with a high-resolution HR-SEM Zeiss Merlin (installed at Tallinn University of Technology) equipped with an In-Lens SE detector for topographic imaging. Measurements were made at an operating voltage of 2 kV.

TEM measurements were performed on SWCNT films in **Publication 3 and 4** by simply transferring the films onto a Lacey carbon-coated TEM-grid. A double aberration-corrected high-resolution TEM FEI Tecnai G2 F20 (HR-TEM) was used to investigate the structure and geometry of the nanotubes. The microscope was operated at an accelerating voltage of 80 kV (**Publication 3**) and 200 kV (**Publication 4**) and with the minimal electron illumination time possible.

3.5 AFM and KPFM

AFM is a well-known technique that can be used to visualize and measure surface structure with unprecedented resolution and accuracy [71]. It is also used to measure force-distance curves, which provide valuable information on local material properties such as elasticity, hardness, Hamaker constant, adhesion and surface charge densities [72]. It can be operated in contact- and non-contact-mode. KPFM is an AFM based tool to measure the local contact potential difference between a conducting AFM tip and the sample, thereby mapping the work function or surface potential of the sample at a high spatial resolution. KPFM has been used extensively to characterize the nano-scale electronic/electrical properties of metal/semiconductor surfaces and semiconductor devices [73].

In **Publication 1**, adhesion force experiments were performed in air using a Bruker MultiMode V8 AFM operating in peak force quantitative nanomechanical mapping mode. Experiments in the inert argon (Ar) environment were performed with Cypher ES AFM (Asylum Research). Prior to each measurements, the probes were calibrated to determine the exact spring constant and displacement in nm. The force-distance curves were collected using each probe on the SWCNT substrate over a grid of 256×256 points^2 in air and 32×32 points^2 in Ar on a 10×10 μm^2 area with the maximum applied force ranging from 5 to 200 nN. From these maps, average adhesion force and deformation were extracted. In **Publications 2 and 3**, KPFM from Asylum Research—Cypher ES was used to test the work function of the SWCNTs, PEDOT:PSS and SWCNTs-PEDOT:PSS composite film. We used Budget Sensors ElectriMulti75-G tips with a spring constant of 1.43 N m^{-1} and the first resonance frequency of 62.081 kHz. The measurements were conducted in an Ar atmosphere glovebox in two pass amplitude modulated-KPFM with the second pass lift height at 35 nm. Highly oriented pyrolytic graphite ZYA was used for calibration prior to the actual measurements.

3.6 Current density-Voltage (*J-V*) measurements

The performance of a solar cell device is evaluated by its current density-voltage (*J-V*) curve under illumination [11]. In Figure 3-2, a typical *J-V* curve of a solar cell is shown. The short-circuit current density J_{SC} is the maximum current density and is obtained in short-circuit condition at V = 0. In the ideal case, it should equal the photo-generated current density J_{ph}, assuming that the dark current at short-circuit conditions can be neglected (close to zero in absence of light). The open-circuit voltage V_{OC} is the maximum voltage

generated by the solar cell and is obtained at J = 0, when no net current is flowing. At any point on the *J-V* curve, the power density that is delivered by the solar cell is defined by $P = V \times J$. The point where the power reaches its maximum P_{max} is called the maximum power point (MPP) with its corresponding current density, J_m, and voltage V_m. The fill factor FF is defined as the ratio of the maximum output power (density) of the solar cell to the product of the short-circuit current (density) J_{sc} times the open-circuit voltage V_{oc} [11]: $FF = \frac{P_{max}}{J_{sc} \times V_{oc}} = \frac{J_m \times V_m}{J_{sc} \times V_{oc}}$ which corresponds to the ratio of the shaded rectangle to the rectangle with the dashed border in Figure 3-2. The fill factor *FF* is linked to the series and shunt resistance R_s and R_{sh} of the solar cell that are calculated from the slope $^{dV}/_{dJ}$ at $V = V_{oc}$ and $V = 0$, respectively. The R_s represents ohmic resistance in the connection wires up to the solar cell and other ohmic resistances within the solar cell between the external connection point and the actual active device; R_{sh} identifies the actual ohmic shunts, and also symbolizes the recombination losses within the solar cell [11]. In principle, for any solar cell the R_s and R_{sh} resistances arise from losses that occur in different regions of the solar cell, and R_s should be as low as possible and R_{sh} is high as possible. *FF* is a very sensitive experimental indication of the quality of a solar cell and it should be used as a complimentary quantity, in addition to the open-circuit voltage V_{oc} to characterize solar cell quality [11]. Finally, the power conversion efficiency (PCE) η is defined as the ratio of maximum power, P_{max}, provided by the solar cell to the power of the incident light P_{ill}, and can be calculated from, $\eta = \frac{P_{max}}{P_{ill}} = \frac{J_{sc} \times V_{oc} \times FF}{P_{ill}}$. Solar cells in this work are characterized by four parameters: J_{sc}, V_{oc}, *FF*, and η.

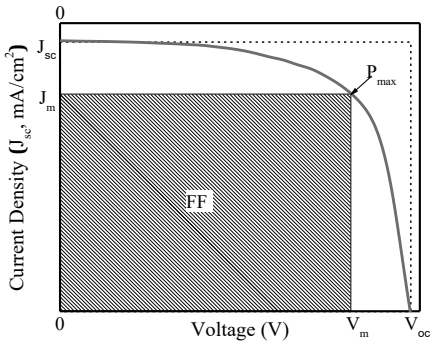

Figure 3-2. Current density-voltage, *J-V* curve of a solar cell and the parameters that can be evaluated: short-circuit current density J_{SC}, open-circuit voltage V_{OC}, current density and voltage at the MPP J_M and V_M, respectively.

The nature of a J-V curve depends on the environmental conditions under which it has been measured. Therefore, standard measurement and reporting conditions have been agreed by the IEC for determining the PCE of the solar cell: an illumination spectrum called Air Mass 1.5G (AM1.5G) with an input power P_{ill} of 1,000 Wm^{-2} and temperature of 25 °C as in IEC 60904-1 and IEC-60904-3 [74,75]. These are referred as 1Sun conditions. The AM1.5G spectrum cannot be completely achieved, hence it is approximated by using a solar simulator in the laboratory [11]. Throughout this thesis, the solar cells are measured using Oriel Sol3A Class AAA, Newport Corporation coupled with a source-meter unit Keithley 2400.

3.7 EQE measurements

A *J-V* curve measurement yields information on the absolute value of the J_{sc} produced in a solar cell. However, this simple measurement does not yield information on the loss mechanisms that are responsible for the fact that not every photon in the solar spectrum contributes to J_{sc}. In the ideal case, every photon with a suitable energy $E > E_g$, where E_g is the band gap of the absorber material, would lead to one electron-hole pair being collected at the terminals of the solar cell. However, in reality this is not the case due to the following reasons: parasitic absorption of the photon themselves, through part of the photons not being absorbed at all within the solar cell, or finally through the recombination of electron-hole pairs. Therefore, we are interested in exploring the reasons for these losses. The EQE method sheds light on this problem through spectral measurement of the J_{scEQE}. The EQE is defined as the number of electrons collected per photon incident on the solar cell according to [11] $EQE = \frac{J_{sc}^{EQE\lambda}}{q \times \phi(\lambda)}$ where $\phi(\lambda)$ is the incident photon flux per time and unit area of the incident light for a certain wavelength and q is the elementary charge. The measurement is performed by illuminating a solar cell with monochromatic light and measuring the photo-generated current for a given wavelength. The measurements are performed in short-circuit conditions. In order to improve the signal-to-noise ratio, the probe light was chopped and changes in photocurrent were detected using a lock-in amplifier.

The EQE of the solar cells in this thesis was measured using a Bentham PVE300 spectral response measurement system. This system used two sources of 75W xenon (300–700 nm) and 100W quartz halogen (700–1800 nm) coupled with a monochromator with a 1.85 × 1.85 mm^2 slit at the output, which provides an approximately 2 × 2 mm^2 monochromatic probe beam on the working plane of a calibrated solar cell. To correct the signal from the lamp

spectrum, calibration was performed on a monocrystalline-Si sample. By integrating the EQE curve over the investigated wavelength range (300 – 800 nm) between λ_1 and λ_2, the current density $J_{sc}^{EQE\lambda}$ of the solar cell can be calculated, with the assumption that the $J_{sc}^{EQE\lambda}$ without light bias will be equal to the J_{sc} from *J-V* curve [76]: $J_{sc}^{EQE\lambda} = -q \int_{\lambda_2}^{\lambda_1} EQE\ (\lambda)\Phi_{ph,\lambda}^{AM1.5} d\lambda$ where q is the elementary charge and $\Phi_{ph,\lambda}^{AM1.5}$ the photon flux density of the AM1.5G solar spectrum.

4. Results and discussion

Each of the following sections describes the main results obtained in Publications 1-4.

In this section, the results obtained in the development of a conductive p-type SWCNT transparent conductor and its application in hybrid heterostructure solar cell based on amorphous silicon are discussed. At the beginning, the results obtained for quantitative measurements of the adhesion of SWCNT films with substrate materials in air and inert Ar atmosphere using atomic force microscopy is presented. It is found that adhesion of SWCNT films depends on the atmospheric conditions under which it is stored and deposited on a substrate material. Following this, a simple fabrication method of hybrid heterostructure solar cells is proposed in which the SWCNT-PEDOT:PSS composite p-type film forms a coupled continuous hybrid heterojunction with a-Si:H absorber. The opto-electrical properties of this composite is extensively characterized and further optimized by introducing multifunctional components like ultrathin MoO_3 and SWCNT fibers. Finally, a rationally designed p-type transparent conductor is proposed with a state-of-the-art sheet resistance of 17 Ω/sq at 90% transmittance. Integrating the developed p-type transparent conductor as a window layer and top electrode on a-Si:H in a nip configuration resulted in a dramatic 16% increase in its power conversion efficiency reaching up to 8.8%.

4.1 Adhesion of SWCNT films (Publication 1)

This section focuses on the systematic investigation of the adhesion properties of SWCNT films with various substrate materials, including SiO_2, ITO, c-Si, a-Si:H, ZrO_2, Pt, PDMS, and SWCNTs for self-adhesion, using atomic force microscopy in air and an inert atmosphere. The results outlined here enable a fundamental understanding of the parameters governing SWCNT film adhesion, and provide a mechanism to improve the adhesion for its efficient usage in opto-electronic devices.

In this work, aerosol synthesized SWCNTs [77,78] are dry-transferred from a nitrocellulose filter [79] to a Si wafer. The film was investigated in an

atomic force microscope by collecting force-distance (F-D) curves between the SWCNT thin film sample and cantilevers coated by a given material, as shown in Figure 4-1.

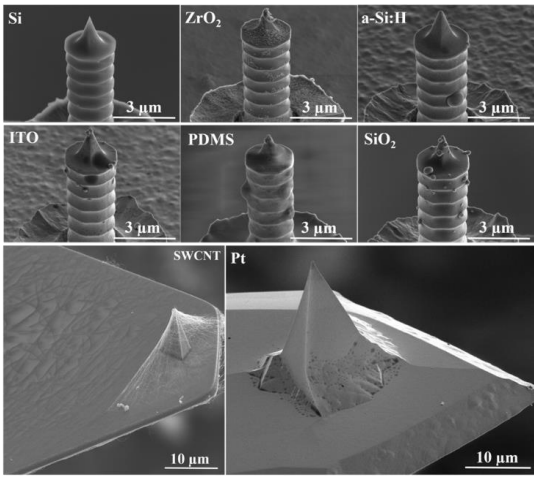

Figure 4-1. Cantilever tips covered with different materials: Si, ZrO_2, a-Si:H, ITO, PDMS, SiO_2, SWCNT, and Pt. Reprinted and adapted with permission from (J. PHYS. CHEM. LETT. 2020, 11, 2, 504-509) under a CC-BY license. Copyright (2020) American Chemical Society.

Collected maps of F-D curves (averaged over 65, 536 measurements in air and 1024 measurements in inert Ar atmosphere) were analyzed by the microscope software. The sample deformation, adhesion force, and peak force values were extracted from F-D curves [80] as shown in Figure 4-2a and 2b. Peak force, or maximum force load, is a predefined set point parameter that is controlled by a microscope feedback loop system.

In order to determine and compare the intrinsic adhesion parameters between SWCNTs and a given material, the measured adhesion force was normalized by the tip-CNT contact area, which is governed by aforementioned force load and tip radius. The Hertz model [81] was used to estimate the tip-surface contact area at the extremum applied force as $S = \pi \times R_{tip} \times h$, where R_{tip} is the tip apex radius and h is the deformation. Within this model it is assumed that the tip apex is a rigid sphere of a certain radius R_{tip}, which was measured on the dimpled aluminum substrate [82], the CNT surface is elastic half space, and the strain is in the elastic limit. The surface roughness is neglected. Despite the fact that in the Hertz model the contact is nonadhesive, it can be accurately applied to adhesive contacts when the adhesive force is small relative to the applied force. The maximum applied force is limited due to the fact that the probe may

drop through a meshy SWCNT surface under a high force loading. As a result, the tip-sample contact area sharply increased due to side contacts of the tip with surrounding CNTs, leading an augmented adhesion force (e.g. Figure 4-2c shows the change in the slope of adhesion force with deformation for ZrO_2 at a peak force of 50 nN as in the inset). With this assumption the moment of the tip drop is inferred from the slope break in the plots shown in Figure 4-2c. With increasing applied force, the adhesion force demonstrates a gradual linear growth. Applying a force of 50 nN resulted in a steep gain in the adhesion force and in some cases cutback of the deformation as shown in Figure 4-2c and corresponding F-D curves in Figure 4-2b. The measured AF as described above [72,80,83] and the calculated SAFD, which is the adhesion force normalized to the contact area, are represented in Figure 4-2d.

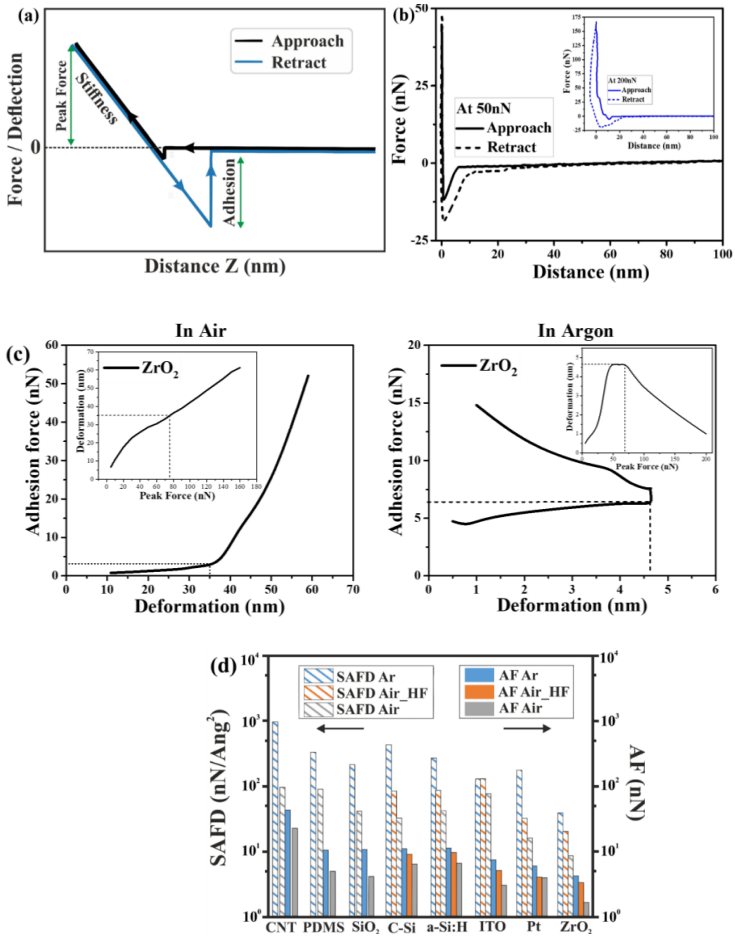

Figure 4-2. (a) Schematic F-D curve; **(b)** Force-distance curves of SWCNT and ZrO_2 at a peak force of 50 nN and 200 nN captured in an inert Ar atmosphere; **(c)** Adhesion force *versus* deformation measured in air and inert Ar atmospheres between a SWCNT film and ZrO_2; and **(d)** Adhesion force (AF) (right

axis, solid bars) and surface adhesion force density (SAFD) (left axis, dashed bars) of SWCNT thin films with various materials. Reprinted and adapted with permission from (J. PHYS. CHEM. LETT. 2020, 11, 2, 504-509) under a CC-BY license. Copyright (2020) American Chemical Society.

For all the studied materials, the normalized adhesion force (adhesion force density) in the inert Ar atmosphere was higher than in ambient air, which can be explained by the difference in the ambient humidity and its influence on SWCNTs as shown by Shandakov *et al.* [84]. RH can affect adhesive properties, especially at the nanoscale, due to the formation of a capillary bridge when RH exceeds a threshold value of roughly 25% [85–87]. The capillary force strongly depends on the sample's local curvature, which affects capillary bridge geometry resulting in a higher adhesion force for a concave surface and a lower adhesion force for a convex surface [85,88]. On hydrophilic surfaces, increasing humidity results an increased pull-off force, whereas on hydrophobic surfaces humidity has a negligible effect [89,90]. Since SWCNTs are hydrophobic [91] and possess a convex surface geometry, the capillary bridge effect is likely to be negligible. Instead, the smaller adhesion force in air is better explained by the reduction of the VdW forces in a polar water medium between the tip and the SWCNT thin film [92,93].

The experimentally measured adhesion force shown in Figure 4-2d can explain the following observations: SWCNT thin films are easily dry-transferred onto a-Si:H, Si, SiO_2, and PDMS in air, while under the same conditions their transfer onto ITO and Pt is complicated and completely failed on ZrO_2. However, the same SWCNT thin films are easily dry-transferred onto all the materials in an inert atmosphere.

To verify that the adhesion force is strongly dependent on the humidity, the a-Si:H, C-Si, ZrO_2, ITO, and Pt coated tips were fluorinated (HF-treated). The process of fluorination (HF-treatment) is well-known to alter the surface properties of materials without changing the bulk characteristics of the pristine material [94,95]. The altered properties may include wettability, adhesion, chemical stability, permeation, electrical conductivity, bio-compatibility, grafting, mechanical behavior, and several others [94]. Dry process fluorination was used, which proceeds spontaneously at room temperature by exposing the samples to HF vapor for 60 seconds. Each tip was calibrated again immediately after HF treatment and the adhesion force measurements were conducted on the same SWCNT thin films in air at a peak force of 50 nN. The measured adhesion forces were recorded for the HF treated tips as illustrated in Figure 4-

2d showing that the adhesion force increased for all HF treated tips. This trend is similar to the adhesion force measurements conducted in the inert atmosphere. Moreover, after the fluorination process SWCNT films can be easily dry-transferred even onto problematic materials, such as ITO, Pt, and ZrO_2.

To summarize, through experimental observations it can be stated that the adhesion is greatly influenced by the environmental conditions and surface functionalization. It is observed that the SWCNT films have a better adhesion in an inert Ar atmosphere. However, the adhesion affected by storing the samples under ambient conditions can be greatly improved by a simple HF-treatment. This provides new insight into the physical mechanisms of SWCNT thin film adhesion that will be useful for its successful implementation in carbon nanotube based devices.

4.2 SWCNT-PEDOT:PSS (Publication 2)

The goal of this section is to utilize the knowledge of SWCNT film adhesion and introduce the synergistic effect of SWCNT film and conductive polymer PEDOT:PSS as effective p-type window layer and electrode in hybrid thin film solar cells using a-Si:H. The results outlined here enable a fundamental understanding of the opto-electrical properties of SWCNT films and composite (SWCNT-PEDOT:PSS) films, and the fabrication of SWCNT/a-Si:H, PEDOT:PSS/a-Si:H, and SWCNT-PEDOT:PSS/a-Si:H hybrid thin film solar cells (HSCs), and introduce PMMA as an effective AR layer.

4.2.1 Optical and electrical properties

Aerosol synthesized SWCNT films [77,79,96] of various transmittance values were characterized for their thickness and sheet resistance. The calculated thickness for a film with a transmittance of T = 90% was about 18 nm (as described in section 3.1) and the measured thickness from AFM was about 19±1 nm. They were dry-transferred [77] onto cleaned micro glass slide (1 × 1 cm^2) and Si wafer (1 × 1 cm^2) to measure their sheet resistance and thickness, respectively. The SWCNTs film transferred on Si wafer was densified using isopropanol and allowed to dry till the solvent evaporation. A scratch was made on the SWCNTs film surface to measure the thickness using AFM. The thickness was averaged over 50 measured points. Figure 4-4 shows the dependence of thickness and sheet resistance on the transmittance at 550 nm. As transmittance increased from 44.4% to 93.5% the sheet resistance increased from 45±2 to 360±2 Ω/□ respectively. In addition, a simple drop-cast of

PEDOT:PSS (2 µl) on the SWCNT films led to a decrease in the sheet resistance by nearly half to 23.4±3.0 and 187.2±4.0 Ω/□ for the SWCNT films with transmittances of T = 44.4% and T = 93.5%, respectively.

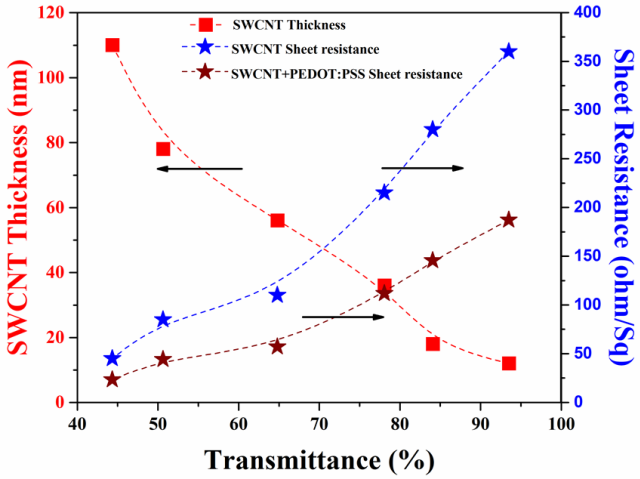

Figure 4-4. Dependence of SWCNT film thickness and sheet resistance on transmittance at 550 nm. Reprinted and adapted with permission from (NANOTECHNOLOGY 29 (2018) 105404 (10PP)) under a CC-BY license. Copyright (2018) IOP Publishing Ltd.

KPFM was used to better understand the decrease in the sheet resistance of SWCNTs with PEDOT:PSS. Three SWCNT film samples with different thicknesses (CNT10, CNT20, and CNT100) were measured with and without PEDOT:PSS. For comparison, a single PEDOT:PSS film was also measured separately. The values of the work function were calculated from KPFM surface potential measurements for the pristine SWCNTs (4.50±0.05 eV), composite film (4.95±0.05 eV), and PEDOT:PSS (5.30±0.05 eV). Fan *et al.* reported similar values of work functions measured by ultraviolet photoemission spectrscopy [97].

The decrease in the sheet resistance of the SWCNT-PEDOT:PSS (composite) film and the increase in its work function compared to the pristine SWCNT film can account for the fact that every single carbon atom are on the surface exposed to the environment. Therefore, any atom/molecule put on a SWCNT cause changes in their electronic structure and charge transfer between the atom/molecule and a nanotube. Therefore, when PEDOT:PSS is injected it filled micropores in the SWCNT film and, that the holes in the PEDOT:PSS patches can transfer to the interconnected SWCNT network consequently, doping the SWCNTs [56,57,97]. As can be seen from Figure 4-5a and 5b, the surface of the composite film is flat and the SWCNT bundled network cannot be

observed clearly from the top of the composite film. This is confirmed by the AFM surface roughness measurements, wherein the pristine SWCNT films showed a RMS roughness of 20 nm, while the composite film RMS roughness was 7 nm. The effect of SWCNT doping can be clearly seen as the work function of the composite film is higher than that of the pristine SWCNTs. Although PEDOT:PSS is less conductive and has a low carrier mobility, the continuous SWCNT network serves as a carrier transport bridge due to its high carrier mobility. Moreover, the net effect of conductivity enhancement is observed to be more pronounced for thinner SWCNT films with PEDOT:PSS. This is probably due to more even distribution of the conducting polymer in the network of SWCNT bundles [97]. This results in a homogeneous coating throughout the thickness of thinner SWCNT films.

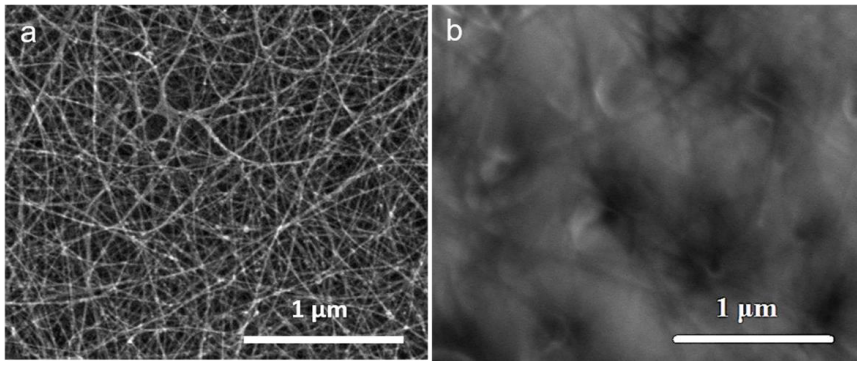

Figure 4-5. Surface morphological SEM image of **(a)** the randomly oriented pristine SWCNT films; **(b)** uniformly coated composite film (PEDOT:PSS - SWCNT film). Reprinted and adapted with permission from (NANOTECHNOLOGY 29 (2018) 105404 (10PP)) under a CC-BY license. Copyright (2018) IOP Publishing Ltd.

4.2.2 Hybrid solar cell fabrication

Figure 4-6a schematically illustrates the HSCs fabrication procedure. The initial layers were fabricated on Corning Eagle XG glass. First, Al:ZnO layers were deposited by DC-sputtering as a transparent back contact for bifacial solar cells. Then, n-doped (30 nm) and intrinsic (i) a-Si:H (300 nm) layers were grown using PECVD using silane, hydrogen and phosphine on top of the Al:ZnO [98]. The i-a-Si:H surface was treated with HF vapor for 140 seconds to remove the native oxide from the surface. Initially, three types of solar cells were fabricated under the same conditions: SWCNT/a-Si:H, PEDOT:PSS/a-Si:H and PEDOT:PSS-SWCNT/a-Si:H.

The SWCNT film was dry-transferred onto an HF-treated i-a-Si:H surface and densified by drop-cast of IPA to ensure a better contact and adhesion to form an SWCNT/a-Si:H HSC. The samples were further heated to 75 ^{o}C in air for 5 minutes to remove the residual solvent.

An electrically conductive PEDOT:PSS polymer, was chosen for application in PEDOT:PSS/i-a-Si:H HSC due to its high hole mobility and environmental stability. PEDOT:PSS was drop-cast or spin coated on top of the i-a-Si:H structures for 90 seconds at 3000 rpm with an acceleration speed of 800 rpm/second from the mixture of aqueous suspension of 5 ml PEDOT:PSS (1.3 wt % Sigma-Aldrich) with glycerine, N-methylpyrrolidone and IPA in a ratio of 1:2:19 respectively. Lastly, to evaporate residues from the solvent and to activate the acceptor states of the polymer [99] the devices were annealed on a hot plate at a temperature of 160^{o} C for 10 minutes.

Subsequent to annealing rectangular shaped front contacts were made at the edges using silver paste on SWCNT/a-Si:H and PEDOT:PSS/a-Si:H HSC structures, respectively. To harden the front contacts the devices were annealed at 160^{o} C for 5 minutes on the hot plate. The active area of the SWCNT/a-Si:H and PEDOT:PSS/a-Si:H HSCs was around 0.5 cm^{2}.

Further, a series of pristine SWCNT films with varying thicknesses (10 nm, 20 nm, 40 nm, 60 nm, 80 nm, and 100 nm) was dry-transferred onto an HF treated i-a-Si:H surface under ambient conditions [77]. A thin PEDOT:PSS layer with a thickness of 50±5 nm was deposited by a simple drop-cast technique to form PEDOT:PSS-SWCNT/a-Si:H HSCs. It was heated on a hot plate in air at 160 ^{o}C for 10 minutes. A thin strip of silver paste was marked at the edges on four sides forming an active HSC area of 0.3 cm^{2}.

The back contact Al:ZnO was reached locally by wet chemical etching of both silicon layers (330 nm) using 6 M KOH solution. Prior to the etching, the samples were heated to 160 ^{o}C in air on a hot plate for 20 minutes. A small volume of 1 µl KOH solution was drop-cast at the edge of the heated samples of the a-Si:H structure. The chemical reaction occurred immediately and the samples were removed from the hot plate after 5 seconds and then rinsed with deionized water. The samples were flushed with nitrogen gas and then heated to 70 ^{o}C in air for 5 minutes to ensure water evaporation. The Al:ZnO resistivity was measured to be 16 Ωcm. The completed architecture of the SWCNT/a-Si:H solar cell device is shown in Figure 4-6b.

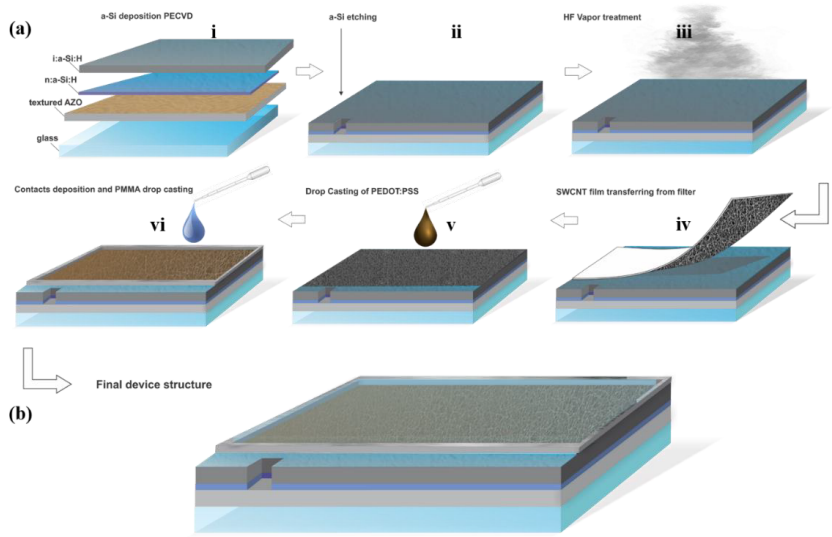

Figure 4-6. (a) Fabrication steps of the HSC process flow: (i) Obtained structure with a-Si:H absorber; (ii) Chemical local etching of a-Si:H to reach Al:ZnO back contact with KOH; (iii) HF vapor treatment of a-Si:H surface for 140 seconds to etch the native oxide; (iv) Dry transfer of SWCNTs onto a HF-treated a-Si:H surface at ambient conditions; (v) Drop-cast of PEDOT:PSS at ambient conditions; (vi) Bordering active area of HSC with silver (silver paste) and final device structure of HSC; and **(b)** Fabricated SWCNT/a-Si:H HSC device. Reprinted and adapted with permission from (NANOTECHNOLOGY 29 (2018) 105404 (10PP)) under a CC-BY license. Copyright (2018) IOP Publishing Ltd.

4.2.3 Solar cell characterization

Synergistic effect of SWCNT-PEDOT:PSS. The *J-V* characteristics of the three types of hybrid solar cells: PEDOT:PSS-SWCNT/a-Si:H, PEDOT:PSS/a-Si:H and SWCNT/a-Si:H were measured in the dark (Figure 4-7a) and under illumination (Figure 4-7b). The *J-V* characteristics of the best performing HSCs measured in the dark clearly reveal the diode properties of all the three types. Analyzing the dark *J-V* curve for all three types of solar cells showed the, PEDOT:PSS-SWCNT/a-Si:H solar cell to exhibit a higher reverse saturation current density (J_o) than the other two solar cells, while their R_{Sh}, R_s and n were nearly the same. The calculated values for the PEDOT:PSS-SWCNT/a-Si:H solar cell were J_o = 3.40±0.01×10^{-4} mA/cm^2, R_p = 75.0±0.5 MΩ/cm^2, R_s = 30.0±0.5 kΩ/cm^2 and n = 1.05±0.05.

J-V curve shifts under illumination showed a typical photovoltaic behavior for all the three hybrid solar cells. However, solar cells with

PEDOT:PSS-SWCNTs and a-Si:H showed more desirable *J-V* characteristics than those with only PEDOT:PSS or SWCNT film. The PEDOT:PSS-SWCNT/a-Si:H solar cell exhibited a better performance: a short-circuit current-density of J_{sc} = 3.56±0.10 mA/cm², an open-circuit voltage of V_{oc} = 0.803±0.003 V, a fill factor of *FF* = 54±3% and a efficiency of η = 1.57±0.03%. Whereas, for the PEDOT:PSS/a-Si:H and SWCNTs/a-Si:H solar cells the equivalent values were J_{sc} = 3.03±0.10 and 2.80±0.10 mA/cm², V_{oc} = 0.710±0.003 and 0.700±0.003 V, *FF* = 40.4±3.0% and 45.2±3.0%, and η = 1.03±0.03% and 1.10±0.03%, respectively (Table 4-1). It is worth noting that the fill factor and open circuit voltage of the PEDOT:PSS-SWCNT/a-Si:H hybrid solar cell exceeded that of amorphous silicon hybrid solar cells using either SWCNTs or conductive polymer [16,17,19,30,31,100]. This can be explained by the introduction of PEDOT:PSS which fills the micropores of the SWCNT film and forms a continuous contact with i-a-Si:H. This leads to the formation of coupled heterojunctions between SWCNT/i-a-Si:H and PEDOT:PSS/i-a-Si:H rather than the usual single-heterojunction between SWCNT/i-a-Si:H, as has been previously reported. Thus, in the PEDOT-SWCNT/i-a-Si:H solar cell, beyond the heterojunctions formed by PEDOT:PSS and SWCNT individually, their combined effect is more important.

EQE measurements of all the three types of hybrid solar cells are shown in Figure 4-7c. The EQE spectrum for PEDOT:PSS-SWCNT/a-Si:H shows a higher EQE saturation value of 24% than for the other two solar cells. Additionally, the SWCNT/a-Si:H solar cell shows a strong blue-shift which may arise from the strong absorbance of SWCNTs near 250 nm [54], phase shift of incident wavelength caused by stack of different refractive index materials in the solar cell. Moreover, in Figure 4.7c for SWCNTs/a-Si:H HSC, the SWCNTs film have a non-uniform contact with underneath a-Si:H creating voids, which are filled with the insertion of PEDOT:PSS in the SWCNTs network (as shown in surface morphological SEM Figure 4-5). This results in a continuous junction with improved interface and reduced recombination. This is clearly noted in Table 4-1, with higher V_{oc} values for PEDOT:PSS-SWCNT/a-Si:H HSC when compared to SWCNTs/a-Si:H or PEDOT:PSS/a-Si:H. However, all three EQE spectra of the hybrid solar cells resemble those of standard a-Si:H solar cell at wavelengths of 300-800 nm. The current densities from the EQE and *J-V* curves match closely for all three solar cells. The sharp decrease in the EQE beyond 700 nm can be attributed to the a-Si:H mobility gap (1.7 eV).

Combining the *J-V* parameters and EQE, the PEDOT:PSS-SWCNT/a-Si:H fabricated solar cell was found to exhibit a state-of-the-art fill factor and

open circuit voltage; while its current density was lower due to an increased absorption of incident photons at the PEDOT:PSS-SWCNT layer (p-layer). Hence, the p-layer needs to be optimized in order to increase absorption and photo-generation of charge carriers in the i-a-Si:H. This will potentially lead to a higher photo-generated current density and efficiency.

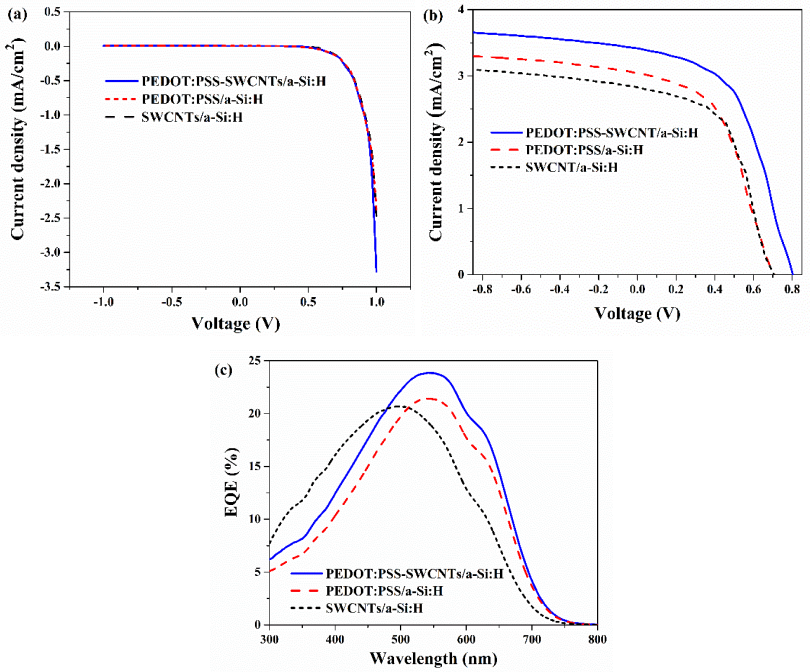

Figure 4-7. (a) dark; and **(b)** photo J-V characteristics of PEDOT:PSS-SWCNT/a-Si:H, PEDOT:PSS/a-Si:H and SWCNT/a-Si:H hybrid solar cells; and **(c)** EQE spectrum. Reprinted and adapted with permission from (PHYS. STATUS SOLIDI B 2018, 255, 1700557) under a CC-BY license. Copyright (2017) WILEY-VCH Verlag GmbH & Co. KGaA, Weinheim.

Table 4-1. *J-V* parameters of the fabricated solar cells: V_{oc}, J_{sc}, *FF*, and PCE (η).

Sample Name	V_{oc} (V)	J_{sc} (mA/cm²)	FF (%)	η (%)
PEDOT:PSS-SWCNT/a-Si:H	0.803	3.56	54.0	1.57
PEDOT:PSS/a-Si:H	0.710	3.03	40.4	1.03
SWCNT/a-Si:H	0.700	2.80	45.2	1.10

Optimization of SWCNT-PEDOT:PSS. The *J-V* characteristics of HSCs fabricated with pristine SWCNTs of different thicknesses (10 nm, 20 nm, 40 nm, 60 nm, 80 nm, and 100 nm samples named CNT10, CNT20, CNT40,

CNT60, CNT80, and CNT100, respectively) are shown in Figure 4-8a and tabulated in Table 4-2. A PCE of η = 2.7±0.3% with a FF of 41.5±3% was achieved for CNT20. As shown in Figure 4-8a, a pristine SWCNT thickness of 19±1 nm was found to be the best in combination with PEDOT:PSS (50±5 nm). A J_{sc} of 7.9±0.1 mA/cm² and V_{oc} of 0.82±0.04 V was measured. Analysis of the dark state curve shown in Figure 4-8a, resulted in J_o = 6.05±0.01×10^{-4} mA/cm², the R_p = 106.0±0.5 MΩ/cm², the R_s = 30±2 kΩ/cm², and the n = 1.10±0.05. The high shunt resistance value together with a very low value of reverse saturation current density and series resistance led to a high PCE of the SWCNT/a-Si:H HSCs. For these measurements, the light was illuminated from the SWCNT side. Moreover, from the *J-V* parameters in Table 4-2, the current density was found to increase from 3.90±0.02 mA/cm² for CNT10 to 7.9±0.1 mA/cm² for CNT20; then to decrease for all the subsequent HSC devices with SWCNT films above 19 nm in thickness. The low current density for CNT10 can be explained by the high resistance of the SWCNTs and PEDOT:PSS. A further increase in the thickness of the SWCNT film beyond 19 nm with PEDOT:PSS yielded a lower current density induced by the decrease in transmittance of SWCNT films. It must be taken into account that the back reflection and the carrier collection on backside were provided with only an Al:ZnO layer and not with a back metal contact. This significantly deteriorated the cell efficiency.

Figure 4-8b shows the experimental EQE spectra corresponding to various SWCNT thicknesses in HSCs. It can be observed that the EQE value decreases with increase in the SWCNT films thickness, with a maximum EQE value of 42% at 514 nm obtained for CNT20. This is caused by lower absorption in the composite film (p-layer) and reduced recombination at the a-Si:H/SWCNT interface in CNT20 compared with any other sample. The current density was calculated from EQE (as described in section 3.7) for all the fabricated solar cells. The current density values of all the solar cells from the *J-V* curve and EQE match closely. For CNT10, CNT40, CNT60, and CNT80 the EQE dramatically decreases for wavelengths shorter than 350 nm indicating a strong surface recombination at the i:a-Si:H/SWCNT interface. A sharp fall in the EQE for all SWCNT film thickness beyond 700 nm can be attributed to the a-Si:H energy gap (1.7 eV). This spectral behavior resembles that of a-Si:H *nip* solar cells, indicating that the photo generation process goes on mainly within the i:a-Si:H.

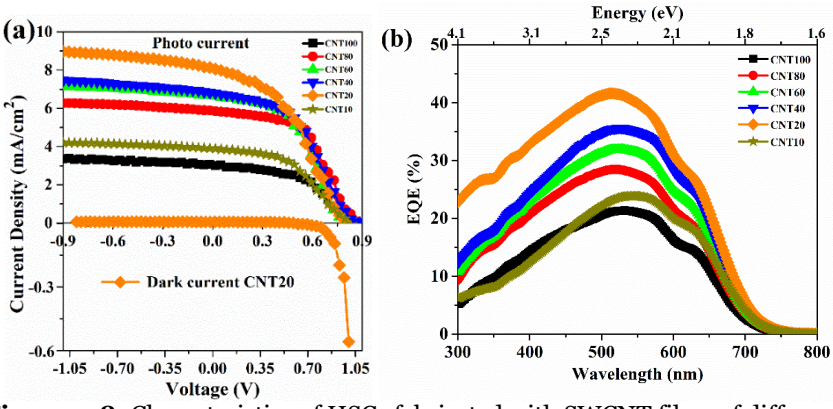

Figure 4-8. Characteristics of HSCs fabricated with SWCNT films of different thicknesses: **(a)** *J-V* curves of the photo and dark current response for CNT20; **(b)** EQE spectra. Reprinted and adapted with permission from (NANOTECHNOLOGY 29 (2018) 105404 (10PP)) under a CC-BY license. Copyright (2018) IOP Publishing Ltd.

Table 4-2. Comparison of *J-V* parameters: V_{oc}, J_{sc}, *FF*, and η of HSCs fabricated with SWCNT films of different thicknesses.

Sample Name	V_{oc} (V)	J_{sc} (mA/cm²)	FF (%)	η (%)
CNT10	0.828	3.90	46.9	1.5
CNT20	0.820	7.90	41.5	2.7
CNT40	0.904	6.80	44.1	2.7
CNT60	0.896	5.90	52.3	2.8
CNT80	0.860	5.70	45.4	2.6
CNT100	0.872	3.04	48.0	1.3

The high current density of CNT20 can also account for the inherent Schottky behavior of SWCNTs due to metallic and semiconducting tubes within its network. Semiconducting SWCNTs have a work function of 4.5 eV with a band gap of 0.5 eV [53] and metallic SWCNTs with a zero bandgap [101] have a work function of nearly 5.0 eV. On forming a composite film with PEDOT:PSS, the SWCNTs network is doped thereby increasing the work function of semiconducting SWCNTs [97]. This is confirmed by the KPFM measurements of the composite film with a work function of 4.95 eV, which is close to the work function of metallic SWCNTs. When this composite film is in contact with i:a-Si:H (Fermi level position of 4.70 eV) [102], the Schottky barrier is reduced across the a-Si:H/SWCNT interface. Moreover, once the thickness of the SWCNT film increases beyond 19 nm, the transmittance decreases, which leads

to a lower absorption and reduced photo generated carriers in the i:a-Si:H. In addition, as the SWCNT film thickness increases, PEDOT:PSS is not evenly distributed along the thickness of the SWCNTs. This possibly results in two recombination centers at the SWCNTs/PEDOT:PSS and SWCNTs/a-Si:H interfaces. Thus, the concentration of the generated hole carriers is lower for CNT40, CNT60, CNT80, and CNT100. It is worth mentioning that in our approach, the optimized composite film of PEDOT:PSS and SWCNT not only increases the effective contact area of a-Si by forming a continuous heterojunction, but also stimulates the holes in PEDOT:PSS to be transferred to the interconnected SWCNT network due to the higher charge carrier mobility and low sheet resistance of SWCNTs along with their one-dimensional axis [103,104]. Thus, PEDOT:PSS and SWCNT together facilitate hole transport from a-Si as shown above in a synergistic effect of SWCNT-PEDOT:PSS. Compared to all the previously reported work [30–32], the combined effect of SWCNTs and PEDOT:PSS was utilized to attain a better and higher J-V characteristics of HSC. This also explains the state-of-the-art performance of the HSCs fabricated in our work.

PMMA as an AR layer. PMMA was used to protect the device from any surface modification under ambient conditions. PMMA has a transmittance close to 100% over a wide wavelength, where a-Si:H generates photo-induced carriers. The fabrication process shown in Figure 6 was modified and the last step of PMMA was added by drop-cast (Figure 4-6a – step vi). 2 µl of PMMA solution was drop-cast onto the fabricated CNT20 device, so that the active area of the cell was uniformly coated. The device was placed on a hot plate at 90 ^{o}C for 20 minutes to ensure solvent evaporation.

Comparison of the *J-V* characteristics of a CNT20 HSC device with PMMA and without PMMA is shown in Figure 4-9a and tabulated in Table 4-3. Compared to the values reported in Table 4-2, the sample CNT20 with PMMA resulted in η = 3.36±0.30%, FF=41.8±3%, J_{sc} = 8.99±0.10 mA/cm^2, and V_{oc} = 0.896±0.040 V. 10% increase in PCE, J_{sc}, and V_{oc} were observed with PMMA. The dark state curve shown in Figure 9a gives the J_o = 8.04±0.01×10^{-4} mA/cm^2, the R_p = 350±1 MΩ/cm^2, the R_s = 21±2 kΩ/cm^2, and n = 1.06±0.03, i.e close to the ideal diode factor, hinting at a reduced carrier recombination. The EQE curves of CNT20 with and without PMMA are shown in Figure 4-9b. The EQE value saturates at 47.1% demonstrating an increase of almost 10%, compared to the device without PMMA. The EQE response is significantly enhanced for a wavelength range from 320 to 640 nm. A sharp increase in the EQE value with

PMMA from 24% at 318 nm to 47% at 500 nm indicates an enhanced light absorption and photo generation in the i-a-Si:H.

Furthermore, the use of PMMA as an AR coating and encapsulant has been a topic of interest and several works have focused on the use of a PMMA layer acting as a broad band ARC over Si-CNT solar cells [105–107]. Hence, diffuse reflectance measurements were carried out to test the effect of PMMA as an ARC in our solar cell. The reflectance spectra of plain a-Si:H, a-Si:H with SWCNTs, a-Si:H with PEDOT:PSS, HSC without PMMA, and HSC with PMMA are shown in Figure 4-9c. The a-Si:H surface with textures exhibits about 20% minimum reflectance ranging from 500–800 nm. The reflection minima of the HSC without PMMA are slightly lower than those of plain a-Si:H, at about 16% in the visible region. The minimum reflectance of a-Si:H with PEDOT:PSS and a-Si:H with SWCNTs is lower than that of plain a-Si:H and is similar to the reflectance of HSC without PMMA. Further, HSC with PMMA shows a reduction to about 4.5% reflectance in the visible region. Consequently, PMMA as an effective ARC increases the light trapping efficiency, producing more photogenerated carriers and thus increasing the current density and HSC efficiency.

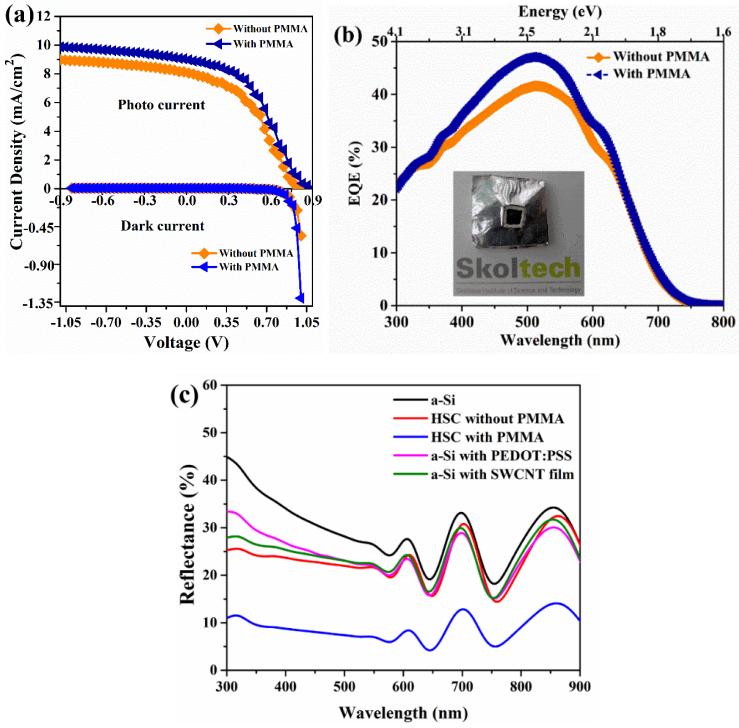

Figure 4-9. Characteristics of HSCs fabricated with CNT20 sample: **(a)** *J-V* curve comparison without and with PMMA for photo and dark current response; **(b)** EQE spectra comparison without and with PMMA; and **(c)** Reflectance spectra of plain a-Si:H, HSC without PMMA, HSC with PMMA, a-

Si:H with PEDOT:PSS, and a-Si:H with SWCNT film. Reprinted and adapted with permission from (NANOTECHNOLOGY 29 (2018) 105404 (10PP)) under a CC-BY license. Copyright (2018) IOP Publishing Ltd.

Table 4-3. Comparison of *J-V* parameters of HSC fabricated with CNT20 sample without and with PMMA.

Conditions	V_{oc} (V)	J_{sc} (mA/cm²)	FF (%)	η (%)
without PMMA	0.820	7.90	41.5	2.70±0.01
with PMMA	0.896	8.99	41.8	3.40±0.01

4.3 Rational design of p-type transparent conductor (Publication 4)

The goal of this section is to utilize the findings of Section 4.2 on the SWCNT-PEDOT:PSS composite and design a novel p-type TCF using MoO_3, doping of the SWCNT film and to introduce SWCNT fibers as potential replacement for traditional metal contacts. This results in a state-of-the-art TCF in a systematic comparison of the optical, electrical, and mechanical properties of different TCF configurations. Finally, HSCs are fabricated introducing a buffer layer between i-a-Si:H/SWCNT-PEDOT:PSS composite and using different TCF configurations: TCF1, TCF2, TCF3, and TCF4.

4.3.1 TCF and solar cell fabrication

Aerosol synthesized SWCNT films were utilized for this work. The doping of SWCNT films was performed using spin-casting of a 15 mM $HAuCl_4$ solution in ethanol [54]. Thin MoO_3 interlayers of about 4 nm were deposited using a thermal evaporation technique in a vacuum at room temperature. Furthermore, a SWCNTs-PEDOT:PSS composite was formed by spin-casting of an electrically conductive PEDOT:PSS on SWCNT films as detailed in Section 4.2. PMMA solution (4 wt.%) in anisole was spin-casted on SWCNT fibers to form the AR layer as detailed in Section 4.2.3.

SWCNT fibers. To utilize the exceptional electrical properties of SWCNTs, the original films were transformed to form self-similar top fiber electrodes. SWCNT films were dry-transferred onto a cleaned glass surface. A drop of IPA was drop-cast on the SWCNT films. The wet film was carefully lifted to make long and narrow SWCNT fibers. Solvent evaporation shrinks the film into a dense fiber (fabrication process is shown in Figures 4-10a-d with a width of 60 to 100 μm after being placed on top of SWCNTs-MoO_3-PEDOT:PSS composite film in a wet-state as shown in Figure 4-10e-f. SWCNTs utilized for

fibers and films were synthesized under the same conditions. Then the wet fiber was placed onto the composite surface and dried to make a conformal contact to the underlying SWCNTs-MoO_3-PEDOT:PSS composite film as seen from Figure 4-10e-f. This flattened shape builds a strong van der Waals interaction between the SWCNT fibers and the composite film, induced by their self-similar structure, thereby completing the TCF.

Solar cell fabrication. For solar cell fabrication, 10×10 cm^2 commercial glass substrates coated with 700 nm textured Al:ZnO as the back contact were used. Both an n-doped a-Si:H layer and intrinsic i-a-Si:H absorber were subsequently grown over the Al:ZnO layer in a multichamber PECVD system von Ardenne CS-400PS at 13.56 MHz as detailed in Section 4.2 [98,108]. After that the substrate was cut into 2.5×2.5 cm^2 individual samples for device fabrication. SWCNT films and fiber top electrodes on a-Si:H (i) define the working area (1 cm^2) of the individual cells. The reference sample was fabricated with a conventional 10 nm p-a-Si window layer and a 90 nm ITO front electrode. The SWCNT/a-Si:H hybrid solar cells were fabricated as described in detail in Section 4.2.2. In brief, partially fabricated a-Si:H thin film solar cells till intrinsic layer were utilized. Ultra-thin MoO_3 (4 nm) was thermally evaporated on a-Si:H (i). Different configurations of developed TCFs (TCF1, TCF2. TCF3 and TCF4) were deposited onto MoO_3 under ambient conditions as a p-type window layer and front electrode to complete the device architecture shown in Figure 4-10e.

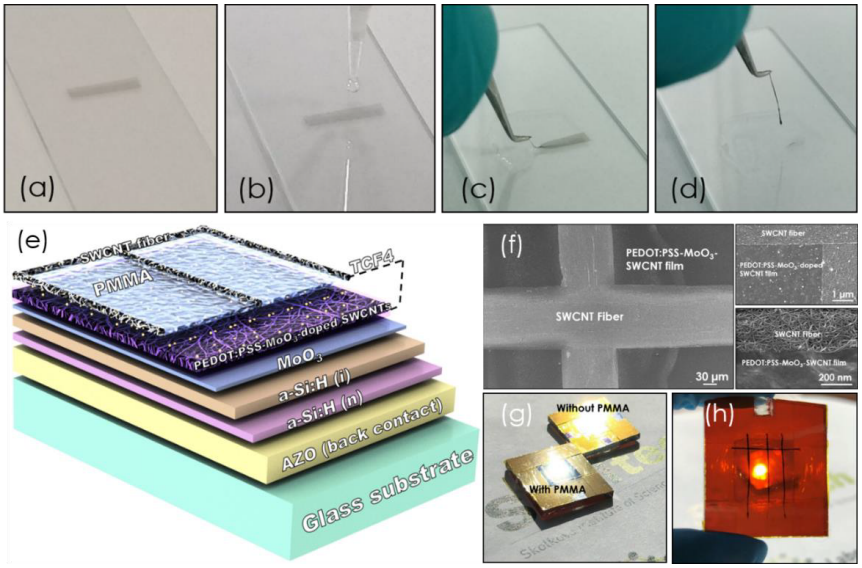

Figure 4-10. SWCNT fiber fabrication process using wet-pulling technique: **(a)** Dry transferred SWCNT film on glass surface; **(b)** Drop-cast of isopropyl alcohol (IPA); **(c)** Self-shrinking of SWCNT film; **(d)** SWCNT fiber formation under the IPA evaporation; **(e)** Solar cell architecture with newly developed transparent electrode TCF4 (from bottom to top): Glass/Al:ZnO/a-Si:H (n)/a-Si:H (i)/MoO_3/SWCNT doped-MoO_3-PEDOT:PSS/SWCNT fibers doped/ PMMA; **(f)** SEM images of SWCNT fibers showing a cross point of two fibers on a cell surface, the PEDOT:PSS-MoO_3-doped SWCNTs composite film and good contact between the composite film and fiber crossed on the cell surface uniformly; **(g)** Fabricated solar cells (with and without PMMA) exposed to sun showing the anti-reflective effect with PMMA coating; and **(h)** Photograph of the fabricated solar cell on a-Si using developed TCF showing its transparency. Reprinted and adapted with permission from (NANO ENERGY 67 (2020) 104183) under a CC-BY license. Copyright (2019) ELSEVIER Ltd.

4.3.2 Optical, electrical, and mechanical properties

All the ingredients utilized to build the p-type multilayer TCFs are listed in Table 4-4. SWCNT films were created using a dry-transfer technique [53], the SWCNT fibers were wet pulled from the film as described above. For doping of the SWCNT films and fibers, $HAuCl_4$ ethanol solution was used. PEDOT:PSS layer was deposited onto SWCNT by a spin-casting technique. MoO_3 was deposited by a thermal evaporation method. The PMMA layer was spin casted onto the surface of the SWCNT fibers.

The surface morphologies of the pristine SWCNT, MoO_3-SWCNT, SWCNTs-MoO_3-PEDOT:PSS and SWCNTs doped -MoO_3-PEDOT:PSS films are shown in Figures 4-11a-d. When deposited onto porous SWCNTs, PEDOT:PSS impregnates the film, which leads to the formation of a homogeneous composite material with a smooth surface. Each successive component added to the composite affected both its optical and electrical properties as shown in Table 4-4. The original SWCNT films had a transmittance of 87% at 550 nm (Figure 4-11e), whereas that of the fiber shrunk from the same SWCNT film was much lower (~2.0%). The reason for the difference is that during the process of being picked up and layed down, the film condensed into a narrow dense fiber with overlapping nanotube bundles depleting most of the incident light (Figure 4-11). Also, for comparison, the optical transmission of PMMA, doped SWCNT film and fiber, SWCNT-MoO_3 and different TCFs (TCF1, TCF2, TCF3 and TCF4 as in Table 4-4) are shown in Figure 4-11. The conductivities (σ in S cm^{-1}) of the SWCNT film and SWCNT fiber were 0.15±0.02 S cm^{-1} and 62.00±7.20 S cm^{-1} respectively, demonstrating the excellent conductivity of the SWCNT fiber. The doped SWCNT films and SWCNT fibers showed a substantial increase in conductivity to 0.51±0.06 S cm^{-1} and 100.00±11.60 S cm^{-1}, respectively. The equivalent sheet resistance (at a transmittance of 90%) [109] of pristine SWCNT film was 364 Ω/sq. Doping of the SWCNT film by $HAuCl_4$ reduced the transmittance value by 2.6%, but also decreased the equivalent sheet resistance to 104 Ω/sq. Similarly, spin casting of PEDOT:PSS on top of the SWCNTs led to a decrease in both the transmittance and sheet resistance of the resulted film. A composite structure containing doped SWCNTs, MoO_3 and PEDOT:PSS revealed a transmittance of 81.2% with an equivalent sheet resistance of 65 Ω/sq. Enhanced optoelectrical properties were observed after SWCNT fibers were added on top of the composite (in a 3 bus bar (3BB) configuration with a distance between parallel fibers of 3 mm as shown in Figures 4-10 and 4-11f), lowering the equivalent sheet resistance to 28 Ω/sq for the non-doped stack SWCNTs-PEDOT:PSS/SWCNT fibers (TCF1). This highlights the fact that SWCNT fibers can also be substituted for traditional metal contacts owing to their high conductivity and simple deposition process as demonstrated here. The deposition of MoO_3 onto the SWCNT surface (TCF2) before adding PEDOT:PSS dropped the value to 22 Ω/sq. A similar observation was reported in several studies indicating that MoO_3 is a stable dopant to SWCNTs [110–112]. A record equivalent sheet resistance of 17 Ω/sq was achieved for a complete structure consisting of $HAuCl_4$ doped SWCNTs with MoO_3 and PEDOT:PSS covered by doped SWCNT fibers (TCF3). To the best of our knowledge, this is

the state-of-the-art equivalent sheet resistance for a transparent electrode based on randomly oriented SWCNT films and for any transparent p-type conductors [113].

Mechanical properties of TCF. The developed transparent p-type conductor showed a high degree of mechanical flexibility in an in-house developed bending setup. The TCF3 on a PI substrate was subjected to 50 000 bending cycles (at bending angles of 20°, 45°, 90° and 180°, which corresponded to radii of curvature of 10, 6.5, 4.5 and 1.6 mm^{-1}). The resistance of the electrodes increased to 0.65 – 5.15%, respectively, and became stable after 23 000 – 40 000 cycles as shown in Figure 4-11g.

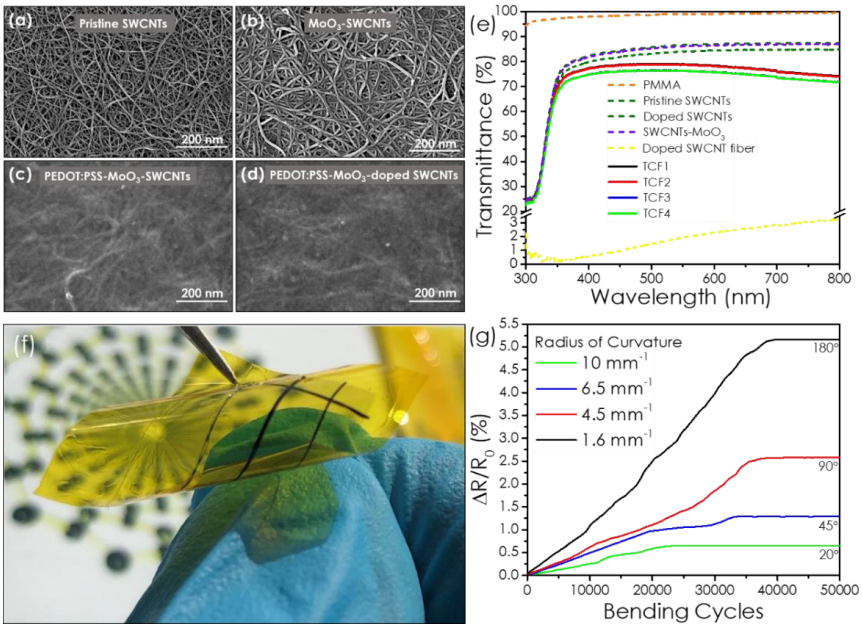

Figure 4-11. Surface morphology of various types of electrodes: **(a)** Pristine SWCNTs; **(b)** MoO_3-SWCNTs; **(c)** PEDOT:PSS-MoO_3-SWCNTs composite; and **(d)** PEDOT:PSS-MoO_3- doped SWCNTs composite. **(e)** Optical transmittance of individual components for the TCFs: pristine and doped SWCNT films, SWCNT+MoO_3, PMMA, and different types of TFCs: TCF1, TCF2, TCF3 and TCF4. For comparison the transmittance spectra of SWCNT fiber and SWCNT fiber doped are also presented; **(f)** A photograph of TCF3 on a polyimide substrate; and **(g)** TCF4 resistance change during 50 000 bending cycles at angles of 20°, 45°, 90° and 180° with the radii of curvature from 10 to 1.6 in mm^{-1}. Reprinted and adapted with permission from (NANO ENERGY 67 (2020) 104183) under a CC-BY license. Copyright (2019) ELSEVIER Ltd.

Table 4-4. Description and comparison of transmittance (%), conductivity, σ (S cm^{-1}), sheet resistance R_s (Ω/sq) and equivalent sheet resistance R_{90} (Ω/sq) of pristine SWCNT film, doped SWCNT film, SWCNT-MoO_3, SWCNT-PEDOT:PSS, SWCNT-MoO_3-PEDOT:PSS, SWCNT doped-MoO_3-PEDOT:PSS, SWCNT fiber, doped SWCNT fiber, TCF1, TCF2, TCF3 and TCF4.

Sample Name	Structure description	T (%)	σ (S cm^{-1})	R_{sh} (Ω/sq)	R_{90} (Ω/sq)
SWCNT film	Thin film of SWCNTs	86.6	0.15± 0.02	128 ± 5.0	364
Doped SWCNT film	Spin-casting of $HAuCl_4$ on SWCNT film.	84.0	0.51 ± 0.06	37 ± 2.0	104
SWCNT-MoO_3	Thermal evaporation of MoO_3 on SWCNT film.	86.2	0.21 ± 0.02	112 ± 3.0	312
SWCNT-PEDOT:PSS	Spin-casting of PEDOT:PSS	84.6	0.59 ± 0.07	76 ± 3.5	205
SWCNT-MoO_3-PEDOT:PSS	Composite structure	83.8	1.00 ± 0.11	49 ± 2.2	123
SWCNT doped-MoO_3-PEDOT:PSS	CNT doped composite structure	81.2	1.82 ± 0.20	27 ± 1.1	65
SWCNT fiber	Narrow fibers from SWCNT film	2.0	62.00 ± 7.20	-	-
Doped SWCNT fiber	Fibers doped with $HAuCl_4$	1.9	100.0 ± 11.6	-	-
TCF1	SWCNTs-PEDOT:PSS/SWCNT fibers	78.9	12.42 ± 1.37	12.0 ± 0.8	28
TCF2	SWCNTs-MoO_3-PEDOT:PSS/SWCNT fibers	78.7	14.90 ± 1.64	10.0 ± 0.4	22
TCF3	SWCNTs doped with $HAuCl_4$-MoO_3-PEDOT:PSS/SWCNT fibers doped with $HAuCl_4$	76.3	24.83 ± 2.73	6.0 ± 0.3	17
TCF4	SWCNTs doped with $HAuCl_4$-MoO_3-PEDOT:PSS/SWCNT fibers doped/PMMA	76.3	24.83 ± 2.73	6.0 ± 0.3	17

4.3.3 Solar cell characterization

To demonstrate the applicability of the developed TCFs, the material was tested as a p-type window layer and a front electrode in hybrid solar cells based on amorphous silicon (the fabricated device picture and the schematics are shown in Figures 4-10). Furthermore, for better extraction of charge carriers and alignment of bands in the solar cell layers, a supplemental ultra-thin MoO_3 layer was added on the a-Si:H(i) surface as both a passivation buffer layer and high work function hole selective contact. The *J-V* characteristics of four different cell types under AM 1.5 and dark conditions are shown in Figures 4-12a and tabulated in Table 4-5. Typical photovoltaic behavior was observed for all types with good correlations between experiments and numerical simulations carried out using AFORS-HET (automat for simulation of heterostructures) software. The TCF1 solar cell *J-V* curve exhibited S-shape behavior with improved short-circuit current density of J_{sc} = 11.93 mA cm^{-2} compared to a solar cell without MoO_3 (Figure 4-12b), open-circuit voltage of V_{oc} = 0.795 V, and fill factor of FF = 41.3%, resulting in PCE = 3.9%.

Subsequently, the TCF2 configuration with MoO_3 on the SWCNT film exhibited J_{sc} = 12.63 mA cm^{-2}, V_{oc} = 0.800 V, and FF = 51.1% (PCE = 5.1%) with no S-shape and elevated photo and dark currents (Figure 4-12a) indicating lower junction and TCF2 resistance (Table 4-4 and Table 4-6).

TCF3 cell showed an ideal *J-V* curve with J_{sc} = 12.83 mA cm^{-2}, improved V_{oc} = 0.870 V and significantly increased FF = 67.4%, resulting in PCE = 7.5%. In the TCF3, doping of the SWCNT films and fibers increases the conductivity of the electrode owing to the reduced Schottky barrier between semiconducting and metallic SWCNTs [56] and increase in the hole concentration, which yields a significant improvement in the short-circuit current and a drop in series resistance (Table 4-5 and 4-6).

Finally, TCF4 devices demonstrated improved characteristics of J_{sc} = 14.11 mA cm^{-2}, V_{oc} = 0.907 V, and FF = 68.0%, leading to a record PCE = 8.3% with a diode ideality factor n = 1.02 (Table 4-6). The increase in the short-circuit current is mainly due to the AR effect of PMMA leading to higher photo-generation current in the a-Si:H layer. Introducing a plain aluminum coated reflective mirror on the back side of the TCF4 solar cell further increased the current density to J_{sc} = 15.03 mA cm^{-2} (Figure 4-12c) and exceeded the state-of-the-art PCE = 8.8%, proving that internal reflection from the back reflector to the cell core further contributes into the increase in absorption by the a-Si:H layer. For comparison, the *J-V* curves of the latter device and the standard reference solar cell (with boron-doped a-Si:H p-type layer and metal contacts)

are shown in Figure 4-12d. A 16% (a net 1.4%) efficiency improvement was seen after integrating the newly developed transparent electrode into the nip-configured a-Si:H solar cell instead of the conventional p-a-Si / TCO front window layer stack. It is to be noted that the reference cells are produced at substrate temperatures less than 200 °C, without any back reflector, texturing and other special processes as carried out for record a-Si:H solar cells.

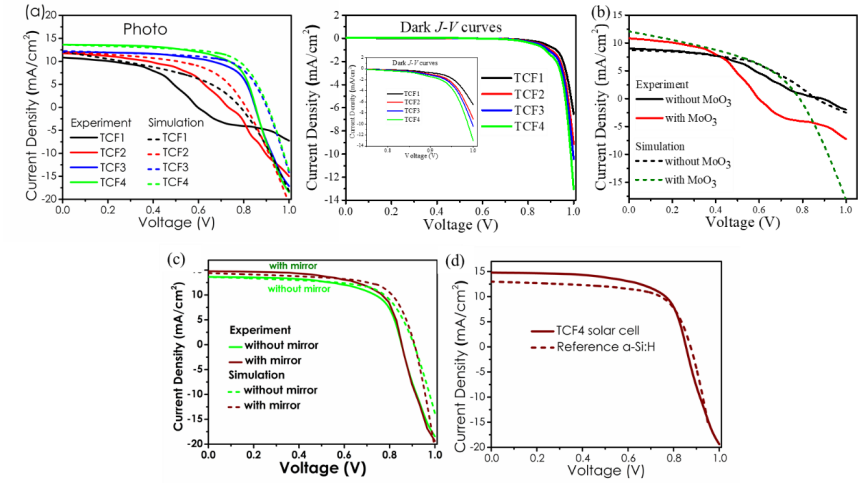

Figure 4-12. Comparison of experimental data and simulations of **(a)** photo and dark J-V curves; **(b)** photo J-V curves with and without MoO_3; (c) photo J-V curves with and without Mirror; and **(d)** J-V curves of TCF4 solar cell and standard reference a-Si:H solar cell. Reprinted and adapted with permission from (NANO ENERGY 67 (2020) 104183) under a CC-BY license. Copyright (2019) ELSEVIER Ltd.

Table 4-5. Comparison of experimental *J-V* parameters of the fabricated solar cells with different TFCs, the standard reference a-Si:H solar cell and the solar cell without MoO_3: V_{oc}, J_{sc}, FF, and η of the fabricated solar cells.

Sample	V_{oc} (V)	J_{sc} (mA/cm²)	FF (%)	η (%)
TCF1	0.795 ±0.024	11.93 ±0.36	41.3 ±1.2	3.90 ±0.2
TCF2	0.800 ±0.024	12.63 ±0.38	51.1 ±1.5	5.10 ±0.2
TCF3	0.870 ±0.026	12.83 ±0.39	67.4 ±2.0	7.50 ±0.2
TCF4	0.907 ±0.027	14.11 ±0.42	68.0 ±2.0	8.30 ±0.3
TCF4 with mirror	0.909 ±0.027	15.03 ±0.45	68.2 ±2.0	8.80 ±0.3
Reference a-Si:H	0.874 ±0.020	12.90 ±0.32	66.5 ±1.5	7.50 ±0.1
Without MoO_3	0.820 ±0.023	7.90 ±0.33	41.5±0.9	2.70 ±0.1

Table 4-6. Calculated *n*, device R_{sr} and R_{sh} of the fabricated solar cells.

Sample	*N*	R_{sr} (Ω cm²)	R_{sh} (Ω cm²)
TCF1	1.10	10.0 ±1.5	175 ±30
TCF2	1.04	6.0±1.0	500 ±85
TCF3	1.03	3.0±0.5	1000 ±171
TCF4	1.02	3.0±0.5	1120 ±192
TCF4 with mirror	1.02	3.0 ±0.5	1120 ±192

The EQE of all solar cell types was measured. Figure 4-13a shows that the EQE value saturated at 75% for the TCF1 and nearly 80% for the TCF2 and TCF3 solar cells in the range from 300 to 800 nm, corresponding to the a-Si:H light absorption wavelength range. This results in an increase in the absolute EQE value by 30% compared to a solar cell without a MoO_3 layer (Figure 4-13b). Increased EQE indicates a reflection drop in the window layer [29], leading to enhanced photocurrent generation (Table 4-7). Moreover, MoO_3 work function (6.5 eV) is higher than that of SWCNTs (4.45 eV), which might lead to additional p-type doping [114]. A drop in the series resistance from 10 Ω cm² (TCF1) to 6 and 3 Ω cm² (for TCF2 and TCF3, respectively) proves the rise of the hole concentration in the SWCNTs coated by MoO_3 (Table 4-6 and Table 4-4). In contrast, the TCF4 solar cell with PMMA exhibited an increase in the EQE value saturated at around 90%, indicating a reduced reflection. Introducing a reflective rear mirror on the back side of a TCF4 solar cell results in broader EQE spectra for wavelengths over 500 nm as shown in Figure 4-13c, clearly demonstrating increased absorption and better optical control in the a-Si:H layer. Also, for comparison the EQE spectra of a standard a-Si:H reference and TCF4 solar cells with reflective mirror is shown in Figure 4-13d. The J_{sc} calculated from EQE spectra and *J-V* parameters for all the solar cell types are in very good agreement with the experiment as shown in Table 4-7, thus validating the performance of all solar cells with the developed transparent conductors.

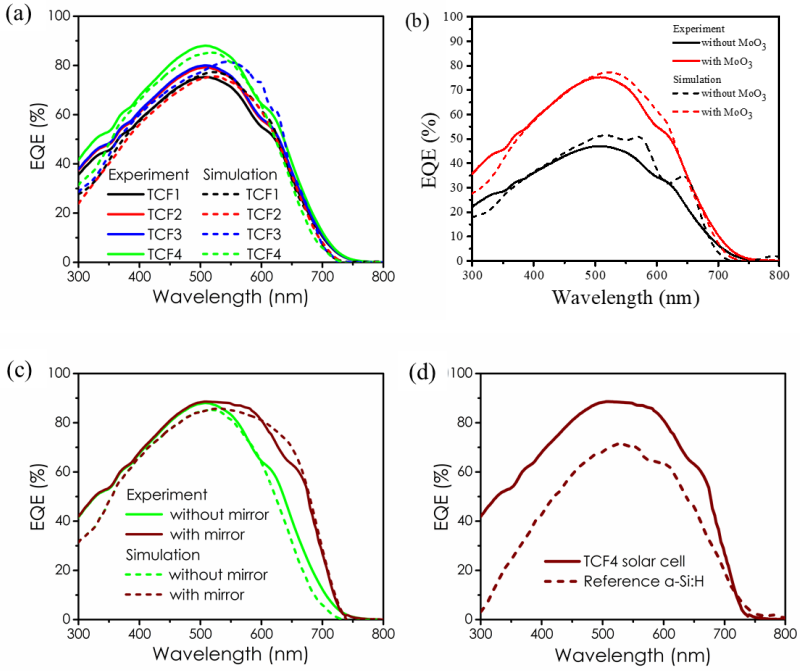

Figure 4-13. Comparison of experimental data and simulations of **(a)** EQE spectra of respective TCF solar cells; **(b)** EQE spectra of without and with MoO_3; **(c)** EQE spectra of without and with mirror; and **(d)** EQE spectra of TCF4 solar cell and standard reference a-Si:H solar cell. Reprinted and adapted with permission from (NANO ENERGY 67 (2020) 104183) under CC-BY license. Copyright (2019) ELSEVIER Ltd.

Table 4-7. Comparison of J_{sc} from *J-V* and EQE curves of the fabricated TCF solar cells and the standard reference a-Si:H solar cell.

Sample	J_{sc} (mA/cm²) from *J-V* curves	J_{sc} (mA/cm²) from EQE
TCF1	11.93 ±0.36	11.80 ±0.36
TCF2	12.63 ±0.38	12.55 ±0.38
TCF3	12.83 ±0.39	12.77 ±0.39
TCF4	14.11 ±0.42	14.09 ±0.42
TCF4 with mirror	15.03 ±0.45	14.97 ±0.45
Reference a-Si:H	12.90 ±0.32	11.90 ±0.32

5. Conclusion and future work

This thesis focusses on the fabrication of hybrid solar cells using SWCNTs film and a-Si:H. The work commenced by investigating the major factors that influence SWCNT film adhesion to various substrate materials. A quantitative evaluation of the SWCNT film adhesion force in air and inert Ar atmospheres with various materials including SiO_2, ITO, Si, a-Si:H, ZrO_2, Pt, PDMS, and SWCNTs for self-adhesion deposited directly on the AFM tips was measured. Quantitative values were derived for the adhesion force from the force-distance curves by estimating the tip-surface contact area according to the Hertz model. Adhesion was found to be greatly influenced by environmental conditions and by surface functionalization. SWCNT thin films have better adhesion in an inert atmosphere. A simple fluorination process greatly improves adhesion, which is affected by sample storage and deposition in ambient air.

This improved understanding of SWCNT film adhesion prompted us to combine it with PEDOT:PSS thus forming a SWCNTs-PEDOT:PSS composite. The, PEDOT:PSS not only filled the micropores but also improved the surface roughness of the SWCNTs. This resulted in a low cost and environmentally friendly fabrication method for hybrid solar cells using SWCNT films and a-Si:H. The window layer and top electrode of this solar cell resulted from the synergistic effect of SWCNTs and PEDOT:PSS forming a composite p-type by simple dry-transfer and spin-casting techniques. The SWCNT-PEDOT:PSS composite p-type with enhanced conductivity provided a continuous hybrid heterojunction with a-Si:H. HSC efficiency increased slightly from 1.6% to 2.7%. A further increase upto 3.4% was recorded by introducing PMMA as an anti-reflective layer. Although significant progress was made in terms of SWCNTs/a-Si:H hybrid solar cell performance, their diode characteristics were still not ideal due to the low conductivity of the SWCNTs-PEDOT:PSS composite and poor p/i interface. This prompted further optimization of the SWCNTs-PEDOT:PSS composite film as a p-type transparent conductor.

Finally, a rational design was proposed for a novel highly efficient flexible transparent p-type conductor, combining the superior properties of doped SWCNTs with PEDOT:PSS, MoO_3 and SWCNT fiber grids into a single

composite material. The use of thin multicomponent layers and the introduction of high-conductive SWCNT fibers resulted in a dramatic improvement of nearly 58% in seet resistance compared to the previous state-of-the-art in p-type TCF development. As demonstrated here, SWCNT fibers can be used to replace traditional metal contacts due to their high conductivity and simple deposition process. A configuration of SWCNTs-MoO_3-PEDOT:PSS/SWCNT fibers resulted in a record equivalent sheet resistance of R_{90} of 17 Ω/sq with a transmittance of 90%, and superior bendability. As a demonstration, the TCFs were used as a combined window layer and front electrode to form hybrid thin film solar cells with an amorphous silicon absorber. An outstanding current of J_{sc} = 15.03 mA/cm² and a record PCE = 8.8% for such thin film solar cells led to an effective 18% improvement over a conventional nip-configured a-Si:H solar cells.

These results are among the best thin film HSCs achieved for SWCNT film and a-Si:H, providing strong evidence that SWCNT-MoO_3-PEDOT:PSS composite p-type films with SWCNT fibers are potential as hole transport window layers and transparent electrodes. It is envisaged that the outcomes of this work will secure the future development of novel p-type TCFs in combination with the use of pure high quality semiconducting or metallic SWCNTs that are aligned with better passivation, improved doping stability of SWCNTs, light trapping schemes and nanostructuring that can potentially improve future photovoltaic devices. Nevertheless, the applications of the novel p-type composite material are not limited to solar cells. Rational design and room-temperature processing broaden the horizon for transparent and flexible electrode implementation in diverse applications in other fields of science and technology.

References

[1] United Nations. World Population Prospects 2019. 2019.

[2] World Urbanization Prospects: The 2018 Revision. 2019. https://doi.org/10.18356/b9e995fe-en.

[3] Energy Information Administration. International Energy Outlook. Outlook 2019. https://doi.org/https://www.eia.gov/outlooks/ieo/pdf/ieo2019.pdf.

[4] IRENA. Renewable Energy Statistics 2019. 2019.

[5] REN 21 Renewables Now. Renewables Global Status Report 2019. 2019.

[6] Louw A, Boyle R, Strahan D, Collins B, Kimmel M, Giannakopoulou E, et al. Global Trends in Renewable Energy Investment 2018. Bloom New Energy Financ 2018. https://doi.org/10.3928/00220124-20081201-03.

[7] OECD/IEA. World Energy Outlook 2018: Electricity. 2018.

[8] Green MA, Dunlop ED, Hohl-Ebinger J, Yoshita M, Kopidakis N, Ho-Baillie AWY. Solar cell efficiency tables (Version 55). Prog Photovoltaics Res Appl 2020. https://doi.org/10.1002/pip.3228.

[9] Yoshikawa K, Kawasaki H, Yoshida W, Irie T, Konishi K, Nakano K, et al. Silicon heterojunction solar cell with interdigitated back contacts for a photoconversion efficiency over 26%. Nat Energy 2017. https://doi.org/10.1038/nenergy.2017.32.

[10] Stuckelberger M, Biron R, Wyrsch N, Haug FJ, Ballif C. Review: Progress in solar cells from hydrogenated amorphous silicon. Renew Sustain Energy Rev 2017. https://doi.org/10.1016/j.rser.2016.11.190.

[11] Shah AV. Thin-film silicon solar cells. 2010. https://doi.org/10.1201/b16327.

[12] Williams EL, Jabbour GE, Wang Q, Shaheen SE, Ginley DS, Schiff EA. Conducting polymer and hydrogenated amorphous silicon hybrid solar cells. Appl Phys Lett 2005. https://doi.org/10.1063/1.2136409.

[13] Gowrishankar V, Scully SR, McGehee MD, Wang Q, Branz HM. Exciton splitting and carrier transport across the amorphous-silicon/ polymer solar cell interface. Appl Phys Lett 2006. https://doi.org/10.1063/1.2408641.

[14] Avasthi S, Lee S, Loo YL, Sturm JC. Role of majority and minority carrier barriers silicon/organic hybrid heterojunction solar cells. Adv Mater 2011. https://doi.org/10.1002/adma.201102712.

[15] Jeong S, Garnett EC, Wang S, Yu Z, Fan S, Brongersma ML, et al. Hybrid silicon nanocone-polymer solar cells. Nano Lett 2012. https://doi.org/10.1021/nl300713x.

[16] Pei Z, Thiyagu S, Jhong MS, Hsieh WS, Cheng SJ, Ho MW, et al. An amorphous silicon random nanocone/polymer hybrid solar cell. Sol Energy Mater Sol Cells 2011. https://doi.org/10.1016/j.solmat.2011.04.021.

[17] Yun MH, Jang JH, Kim KM, Song HE, Lee JC, Kim JY. A hybrid solar cell

fabricated using amorphous silicon and a fullerene derivative. Phys Chem Chem Phys 2013. https://doi.org/10.1039/c3cp53493f.

[18] Liu R, Lee ST, Sun B. 13.8% Efficiency Hybrid Si/Organic Heterojunction Solar Cells with MoO3 Film as Antireflection and Inversion Induced Layer. Adv Mater 2014. https://doi.org/10.1002/adma.201402076.

[19] Schaefer S, Albrecht S, Neher D, Schulze TF, Conrad E, Korte L, et al. Electric Field Distribution in Hybrid Solar Cells Comprising an Organic Donor Polymer and Amorphous Silicon. Org Photonics Photovoltaics 2014. https://doi.org/10.2478/oph-2014-0004.

[20] Angmo D, Krebs FC. Flexible ITO-free polymer solar cells. J Appl Polym Sci 2013. https://doi.org/10.1002/app.38854.

[21] Kim J, Hong Z, Li G, Song T Bin, Chey J, Lee YS, et al. 10.5% efficient polymer and amorphous silicon hybrid tandem photovoltaic cell. Nat Commun 2015. https://doi.org/10.1038/ncomms7391.

[22] Tan H, Furlan A, Li W, Arapov K, Santbergen R, Wienk MM, et al. Highly Efficient Hybrid Polymer and Amorphous Silicon Multijunction Solar Cells with Effective Optical Management. Adv Mater 2016. https://doi.org/10.1002/adma.201504483.

[23] Lu S, Sun Y, Ren K, Liu K, Wang Z, Qu S. Recent development in ITO-free flexible polymer solar cells. Polymers (Basel) 2017. https://doi.org/10.3390/polym10010005.

[24] Jäckle S, Liebhaber M, Gersmann C, Mews M, Jäger K, Christiansen S, et al. Potential of PEDOT:PSS as a hole selective front contact for silicon heterojunction solar cells. Sci Rep 2017. https://doi.org/10.1038/s41598-017-01946-3.

[25] Jeon I, Xiang R, Shawky A, Matsuo Y, Maruyama S. Single-Walled Carbon Nanotubes in Emerging Solar Cells: Synthesis and Electrode Applications. Adv Energy Mater 2019. https://doi.org/10.1002/aenm.201801312.

[26] Jeon I, Matsuo Y, Maruyama S. Single-Walled Carbon Nanotubes in Solar Cells. Top Curr Chem 2018. https://doi.org/10.1007/s41061-017-0181-0.

[27] Jariwala D, Sangwan VK, Lauhon LJ, Marks TJ, Hersam MC. Carbon nanomaterials for electronics, optoelectronics, photovoltaics, and sensing. Chem Soc Rev 2013. https://doi.org/10.1039/c2cs35335k.

[28] Xu W, Wu S, Li X, Zou M, Yang L, Zhang Z, et al. High-Efficiency Large-Area Carbon Nanotube-Silicon Solar Cells. Adv Energy Mater 2016. https://doi.org/10.1002/aenm.201600095.

[29] Wang F, Kozawa D, Miyauchi Y, Hiraoka K, Mouri S, Ohno Y, et al. Considerably improved photovoltaic performance of carbon nanotube-based solar cells using metal oxide layers. Nat Commun 2015. https://doi.org/10.1038/ncomms7305.

[30] Schriver M, Regan W, Loster M, Zettl A. Carbon nanostructure-aSi:H photovoltaic cells with high open-circuit voltage fabricated without dopants. Solid State Commun 2010;150:561–3.

https://doi.org/10.1016/j.ssc.2010.01.013.

[31] Del Gobbo S, Castrucci P, Scarselli M, Camilli L, De Crescenzi M, Mariucci L, et al. Carbon nanotube semitransparent electrodes for amorphous silicon based photovoltaic devices. Appl Phys Lett 2011;98:1–4. https://doi.org/10.1063/1.3588352.

[32] Funde AM, Nasibulin AG, Syed HG, Anisimov AS, Tsapenko A, Lund P, et al. Carbon nanotube-amorphous silicon hybrid solar cell with improved conversion efficiency. Nanotechnology 2016. https://doi.org/10.1088/0957-4484/27/18/185401.

[33] Publications B, A Jorio; G Dresselhaus; M S Dresselhaus. Topics in Applied Physics Volume 111. vol. 111. 2008.

[34] Iijima S, Ichihashi T. Single-shell carbon nanotubes of 1-nm diameter. Nature 1993. https://doi.org/10.1038/363603a0.

[35] Wright M, Uddin A. Organic-inorganic hybrid solar cells: A comparative review. Sol Energy Mater Sol Cells 2012. https://doi.org/10.1016/j.solmat.2012.07.006.

[36] Alet P-J, Palacin S, Roca I Cabarrocas P, Kalache B, Firon M, de Bettignies R. Hybrid solar cells based on thin-film silicon and P3HT. Eur Phys J Appl Phys 2006. https://doi.org/10.1051/epjap:2006145.

[37] Kymakis E, Amaratunga GAJ. Solar cells based on composites of donor conjugated polymers and carbon nanotubes. Org. Photovoltaics Mech. Mater. Devices, 2017. https://doi.org/10.1201/9781420026351.

[38] Landi BJ, Raffaelle RP, Castro SL, Bailey SG. Single-wall carbon nanotube-polymer solar cells. Prog. Photovoltaics Res. Appl., 2005. https://doi.org/10.1002/pip.604.

[39] Kymakis E, Klapsis G, Koudoumas E, Stratakis E, Kornilios N, Vidakis N, et al. THE EUROPEAN PHYSICAL JOURNAL Carbon nanotube/PEDOT:PSS electrodes for organic photovoltaics. J Appl PhysNp Nanoparticles Polym 2007. https://doi.org/10.1051/epjap:2006148.

[40] Hu X, Hou P, Liu C, Cheng H. Carbon nanotube/silicon heterojunctions for photovoltaic applications. Nano Mater Sci 2019:1–17. https://doi.org/10.1016/j.nanoms.2019.03.001.

[41] Street RA. Hydrogenated Amorphous Silicon. 1991. https://doi.org/10.1017/cbo9780511525247.

[42] Luque A, Hegedus S. Handbook of Photovoltaic Science and Engineering. 2011. https://doi.org/10.1002/9780470974704.

[43] DeWolf S, Descoeudres A, Holman ZC, Ballif C. High-efficiency silicon heterojunction solar cells: A review. Green 2012. https://doi.org/10.1515/green-2011-0018.

[44] Matsuda A. Thin-film silicon - Growth process and solar cell application. Japanese J Appl Physics, Part 1 Regul Pap Short Notes Rev Pap 2004. https://doi.org/10.1143/JJAP.43.7909.

[45] Rockett A. The materials science of semiconductors. 2008.

https://doi.org/10.1007/978-0-387-68650-9.

[46] Staebler DL, Wronski CR. Reversible conductivity changes in discharge-produced amorphous Si. Appl Phys Lett 1977. https://doi.org/10.1063/1.89674.

[47] Stutzmann M, Jackson WB, Tsai CC. Light-induced metastable defects in hydrogenated amorphous silicon: A systematic study. Phys Rev B 1985. https://doi.org/10.1103/PhysRevB.32.23.

[48] Proctor JE, Armada DAM, Vijayaraghavan A. An introduction to graphene and carbon nanotubes. 2017. https://doi.org/10.1201/9781315368191.

[49] Moisala A, Nasibulin AG, Brown DP, Jiang H, Khriachtchev L, Kauppinen EI. Single-walled carbon nanotube synthesis using ferrocene and iron pentacarbonyl in a laminar flow reactor. Chem Eng Sci 2006. https://doi.org/10.1016/j.ces.2006.02.020.

[50] Liao Y, Hussain A, Laiho P, Zhang Q, Tian Y, Wei N, et al. Tuning Geometry of SWCNTs by CO2 in Floating Catalyst CVD for High-Performance Transparent Conductive Films. Adv Mater Interfaces 2018. https://doi.org/10.1002/admi.201801209.

[51] Anisimov AS, Nasibulin AG, Jiang H, Launois P, Cambedouzou J, Shandakov SD, et al. Mechanistic investigations of single-walled carbon nanotube synthesis by ferrocene vapor decomposition in carbon monoxide. Carbon N Y 2010. https://doi.org/10.1016/j.carbon.2009.09.040.

[52] Nasibulin AG, Moisala A, Brown DP, Jiang H, Kauppinen EI. A novel aerosol method for single walled carbon nanotube synthesis. Chem Phys Lett 2005. https://doi.org/10.1016/j.cplett.2004.12.040.

[53] Kaskela A, Nasibulin AG, Timmermans MY, Aitchison B, Papadimitratos A, Tian Y, et al. Aerosol-synthesized SWCNT networks with tunable conductivity and transparency by a dry transfer technique. Nano Lett 2010. https://doi.org/10.1021/nl101680s.

[54] Tsapenko AP, Goldt AE, Shulga E, Popov ZI, Maslakov KI, Anisimov AS, et al. Highly conductive and transparent films of HAuCl4-doped single-walled carbon nanotubes for flexible applications. Carbon N Y 2018. https://doi.org/10.1016/j.carbon.2018.01.016.

[55] Tsapenko AP, Romanov SA, Satco DA, Krasnikov D V., Rajanna PM, Danilson M, et al. Aerosol-Assisted Fine-Tuning of Optoelectrical Properties of SWCNT Films. J Phys Chem Lett 2019. https://doi.org/10.1021/acs.jpclett.9b01498.

[56] Ki KK, Jung JB, Hyeon KP, Soo MK, Geng HZ, Kyung AP, et al. Fermi level engineering of single-walled carbon nanotubes by AuCl 3 doping. J Am Chem Soc 2008. https://doi.org/10.1021/ja8038689.

[57] Kim KK, Yoon SM, Park HK, Shin HJ, Kim SM, Bae JJ, et al. Doping strategy of carbon nanotubes with redox chemistry. New J Chem 2010. https://doi.org/10.1039/conj00138d.

[58] Elschner A, Kirchmeyer S, Lövenich W, Merker U, Reuter K. PEDOT: Principles and applications of an intrinsically conductive polyme. 2010.

https://doi.org/10.1201/b10318.

[59] Fan X, Nie W, Tsai H, Wang N, Huang H, Cheng Y, et al. PEDOT:PSS for Flexible and Stretchable Electronics: Modifications, Strategies, and Applications. Adv Sci 2019. https://doi.org/10.1002/advs.201900813.

[60] Il Park S, Jae Baik S, Im JS, Fang L, Jeon JW, Su Lim K. Towards a high efficiency amorphous silicon solar cell using molybdenum oxide as a window layer instead of conventional p-type amorphous silicon carbide. Appl Phys Lett 2011. https://doi.org/10.1063/1.3624591.

[61] Battaglia C, Yin X, Zheng M, Sharp ID, Chen T, McDonnell S, et al. Hole selective MoOxcontact for silicon solar cells. Nano Lett 2014. https://doi.org/10.1021/nl404389u.

[62] Gerling LG, Mahato S, Morales-Vilches A, Masmitja G, Ortega P, Voz C, et al. Transition metal oxides as hole-selective contacts in silicon heterojunctions solar cells. Sol Energy Mater Sol Cells 2016. https://doi.org/10.1016/j.solmat.2015.08.028.

[63] Guo Y, Robertson J. Origin of the high work function and high conductivity of MoO3. Appl Phys Lett 2014. https://doi.org/10.1063/1.4903538.

[64] Schulz P, Tiepelt JO, Christians JA, Levine I, Edri E, Sanehira EM, et al. High-work-function molybdenum oxide hole extraction contacts in hybrid organic-inorganic perovskite solar cells. ACS Appl Mater Interfaces 2016. https://doi.org/10.1021/acsami.6b10898.

[65] Jiang Y, Li C, Liu H, Qin R, Ma H. Poly(3,4-ethylenedioxythiophene):poly(styrenesulfonate)(PEDOT:PSS)-molybdenum oxide composite films as hole conductors for efficient planar perovskite solar cells. J Mater Chem A 2016. https://doi.org/10.1039/c6ta03658a.

[66] Li X, Jung Y, Huang JS, Goh T, Taylor AD. Device area scale-up and improvement of SWNT/Si solar cells using silver nanowires. Adv Energy Mater 2014. https://doi.org/10.1002/aenm.201400186.

[67] Jeong S, Garnett EC, Wang S, Yu Z, Fan S, Brongersma ML, et al. Hybrid silicon nanocone-polymer solar cells. Nano Lett 2012. https://doi.org/10.1021/nl300713x.

[68] Mikheev GM, Nasibulin AG, Zonov RG, Kaskela A, Kauppinen EI. Photon-Drag Effect in Single-Walled Carbon Nanotube Films. Nano Lett 2012;12:77–83. https://doi.org/10.1021/nl203003p.

[69] Watts JF, Wolstenholme J. An Introduction to Surface Analysis by XPS and AES. 2019. https://doi.org/10.1002/9781119417651.

[70] Sze SM, Ng KK. Physics of Semiconductor Devices: Third Edition. 2006. https://doi.org/10.1002/9780470068328.

[71] Eaton P, West P. Atomic Force Microscopy. 2010. https://doi.org/10.1093/acprof:oso/9780199570454.001.0001.

[72] Butt HJ, Cappella B, Kappl M. Force measurements with the atomic force microscope: Technique, interpretation and applications. Surf Sci Rep

2005;59:1–152. https://doi.org/10.1016/j.surfrep.2005.08.003.

[73] Melitz W, Shen J, Kummel AC, Lee S. Kelvin probe force microscopy and its application. Surf Sci Rep 2011. https://doi.org/10.1016/j.surfrep.2010.10.001.

[74] Wohlgemuth JH. Standards for pv modules and components – Recent developments and challenges. 27th Eur Photovolt Sol Energy Conf Exhib 2012.

[75] IEC. IEC 60904-3 Edition 2.0 Part 3: Measurement principles for terrestrial photovoltaic (PV) solar devices with reference spectral irradiance data. 2008. https://doi.org/10.3403/01776181.

[76] Abou-Ras D, Kirchartz T, Rau U. Advanced Characterization Techniques for Thin Film Solar Cells: Second Edition. 2016. https://doi.org/10.1002/9783527699025.

[77] Nasibulin AG, Kaskela A, Mustonen K, Anisimov AS, Ruiz V, Kivistö S, et al. Multifunctional free-standing single-walled carbon nanotube films. ACS Nano 2011. https://doi.org/10.1021/nn200338r.

[78] Moisala A, Nasibulin AG, Brown DP, Jiang H, Khriachtchev L, Kauppinen EI. Single-walled carbon nanotube synthesis using ferrocene and iron pentacarbonyl in a laminar flow reactor. Chem Eng Sci 2006. https://doi.org/10.1016/j.ces.2006.02.020.

[79] Kaskela A, Nasibulin AG, Timmermans MY, Aitchison B, Papadimitratos A, Tian Y, et al. Aerosol-synthesized SWCNT networks with tunable conductivity and transparency by a dry transfer technique. Nano Lett 2010. https://doi.org/10.1021/nl101680s.

[80] Cappella B, Baschieri P, Frediani C, Miccoli P, Ascoli C. Force-distance curves by AFM. IEEE Eng Med Biol Mag 1997;16:58–65. https://doi.org/10.1109/51.582177.

[81] Meyer E, Gyalog T, Overney RM, Dransfeld K. Nanoscience: Friction and Rheology on the Nanometer Scale. 2012. https://doi.org/10.1142/3026.

[82] Dremov V, Fedoseev V, Fedorov P, Grebenko A. Fast and reliable method of conductive carbon nanotube-probe fabrication for scanning probe microscopy. Rev Sci Instrum 2015. https://doi.org/10.1063/1.4921323.

[83] Adam Moser, Kevin Range and DMY. Adhesion Force Measurements Using an Atomic Force Microscope Upgraded with a Linear Position Sensitive Detector. Bone 2008;23:1–7. https://doi.org/10.1038/jid.2014.371.

[84] Shandakov SD, Lomakin M V., Nasibulin AG. The effect of the environment on the electronic properties of single-walled carbon nanotubes. Tech Phys Lett 2016. https://doi.org/10.1134/S1063785016110080.

[85] Paajanen M, Katainen J, Pakarinen OH, Foster AS, Lahtinen J. Experimental humidity dependency of small particle adhesion on silica and titania. J Colloid Interface Sci 2006. https://doi.org/10.1016/j.jcis.2006.09.017.

[86] Weeks BL, Vaughn MW, Deyoreo JJ. Direct imaging of meniscus formation in atomic force microscopy using environmental scanning electron microscopy. Langmuir 2005. https://doi.org/10.1021/la0512087.

[87] Xiao X, Qian L. Investigation of humidity-dependent capillary force. Langmuir 2000. https://doi.org/10.1021/la0007700.

[88] Sirghi L, Nakagiri N, Sugisaki K, Sugimura H, Takai O. Effect of sample topography on adhesive force in atomic force spectroscopy measurements in air. Langmuir 2000. https://doi.org/10.1021/la000392n.

[89] Jones R, Pollock HM, Cleaver JAS, Hodges CS. Adhesion forces between glass and silicon surfaces in air studied by AFM: Effects of relative humidity, particle size, roughness, and surface treatment. Langmuir 2002. https://doi.org/10.1021/la0259196.

[90] Fukunishi A, Mori Y. Adhesion force between particles and substrate in a humid atmosphere studied by atomic force microscopy. Adv Powder Technol 2006. https://doi.org/10.1163/156855206778440552.

[91] Kyakuno H, Fukasawa M, Ichimura R, Matsuda K, Nakai Y, Miyata Y, et al. Diameter-dependent hydrophobicity in carbon nanotubes. J Chem Phys 2016. https://doi.org/10.1063/1.4960609.

[92] McLachlan a. D. Retarded Dispersion Forces in Dielectrics at Finite Temperatures. Proc R Soc A Math Phys Eng Sci 1963. https://doi.org/10.1098/rspa.1963.0115.

[93] Leite FL, Bueno CC, Da Róz AL, Ziemath EC, Oliveira ON. Theoretical models for surface forces and adhesion and their measurement using atomic force microscopy. Int J Mol Sci 2012. https://doi.org/10.3390/ijms131012773.

[94] Tressaud A, Durand E, Labrugère C, Kharitonov AP, Kharitonova LN. Modification of surface properties of carbon-based and polymeric materials through fluorination routes: From fundamental research to industrial applications. J Fluor Chem 2007. https://doi.org/10.1016/j.jfluchem.2006.12.015.

[95] Liang T, Neumann CN, Ritter T. Introduction of fluorine and fluorine-containing functional groups. Angew Chemie - Int Ed 2013. https://doi.org/10.1002/anie.201206566.

[96] Tian Y, Timmermans MY, Kivistö S, Nasibulin AG, Zhu Z, Jiang H, et al. Tailoring the diameter of single-walled carbon nanotubes for optical applications. Nano Res 2011. https://doi.org/10.1007/s12274-011-0137-6.

[97] Fan Q, Zhang Q, Zhou W, Xia X, Yang F, Zhang N, et al. Novel approach to enhance efficiency of hybrid silicon-based solar cells via synergistic effects of polymer and carbon nanotube composite film. Nano Energy 2017. https://doi.org/10.1016/j.nanoen.2017.02.003.

[98] Neumüller A, Bereznev S, Ewert M, Volobujeva O, Sergeev O, Falta J, et al. Carrier collection losses in interface passivated amorphous silicon thin-film solar cells. Appl Phys Lett 2016. https://doi.org/10.1063/1.4959995.

[99] Vitoratos E, Sakkopoulos S, Paliatsas N, Emmanouil K, Choulis SA. Conductivity Degradation Study of PEDOT: PSS Films under Heat Treatment in Helium and Atmospheric Air. Open J Org Polym Mater 2012.

https://doi.org/10.4236/ojopm.2012.21002.

[100] Dosenovicova D, Maricheva J, Neumüller A, Sergeev O, Volobujeva O, Nasibulin AG, et al. Selective photoelectrochemical deposition of polypyrrole onto hydrogenated a-Si for optoelectronic applications. Mater Sci Semicond Process 2017. https://doi.org/10.1016/j.mssp.2017.05.028.

[101] Deslippe J, Spataru CD, Prendergast D, Louie SG. Bound excitons in metallic single-walled carbon nanotubes. Nano Lett 2007. https://doi.org/10.1021/nl070577f.

[102] Schropp REI, Zeman M. Amorphous and Microcrystalline Silicon Solar Cells: Modeling, Materials and Device Technology. 1998. https://doi.org/10.1007/978-1-4615-5631-2.

[103] Fuhrer MS, Kim BM, Dürkop T, Brintlinger T. High-Mobility Nanotube Transistor Memory. Nano Lett 2002. https://doi.org/10.1021/nl0255770.

[104] Snow ES, Campbell PM, Ancona MG, Novak JP. High-mobility carbon-nanotube thin-film transistors on a polymeric substrate. Appl Phys Lett 2005. https://doi.org/10.1063/1.1854721.

[105] Li R, Di J, Yong Z, Sun B, Li Q. Polymethylmethacrylate coating on aligned carbon nanotube-silicon solar cells for performance improvement. J Mater Chem A 2014. https://doi.org/10.1039/c3ta14625a.

[106] Li X, Yu X, Han Y. Polymer thin films for antireflection coatings. J Mater Chem C 2013. https://doi.org/10.1039/c2tc00529h.

[107] Yu LP, Tune DD, Shearer CJ, Shapter JG. Implementation of antireflection layers for improved efficiency of carbon nanotube-silicon heterojunction solar cells. Sol Energy 2015. https://doi.org/10.1016/j.solener.2015.06.014.

[108] Neumüller A, Sergeev O, Heise SJ, Bereznev S, Volobujeva O, Salas JFL, et al. Improved amorphous silicon passivation layer for heterojunction solar cells with post-deposition plasma treatment. Nano Energy 2018. https://doi.org/10.1016/j.nanoen.2017.11.053.

[109] Anoshkin I V., Nasibulin AG, Tian Y, Liu B, Jiang H, Kauppinen EI. Hybrid carbon source for single-walled carbon nanotube synthesis by aerosol CVD method. Carbon N Y 2014. https://doi.org/10.1016/j.carbon.2014.06.057.

[110] Jeon I, Cui K, Chiba T, Anisimov A, Nasibulin AG, Kauppinen EI, et al. Direct and Dry Deposited Single-Walled Carbon Nanotube Films Doped with MoOx as Electron-Blocking Transparent Electrodes for Flexible Organic Solar Cells. J Am Chem Soc 2015. https://doi.org/10.1021/jacs.5b03739.

[111] Esconjauregui S, D'Arsié L, Guo Y, Yang J, Sugime H, Caneva S, et al. Efficient Transfer Doping of Carbon Nanotube Forests by MoO3. ACS Nano 2015. https://doi.org/10.1021/acsnano.5b04644.

[112] Çolak F, Dalkiliç Z, Tabatabaei A, Atlibatur R, Çolak, Arici E, et al. MoOx doped single-walled carbon nanotube films as hole transport layer for organic solar cells. Acta Phys. Pol. A, 2017. https://doi.org/10.12693/APhysPolA.131.474.

[113] Zhang KHL, Xi K, Blamire MG, Egdell RG. *P* -type transparent conducting

oxides. J Phys Condens Matter 2016. https://doi.org/10.1088/0953-8984/28/38/383002.

[114] Hellstrom SL, Vosgueritchian M, Stoltenberg RM, Irfan I, Hammock M, Wang YB, et al. Strong and stable doping of carbon nanotubes and graphene by MoO x for transparent electrodes. Nano Lett 2012. https://doi.org/10.1021/nl301207e.

Most of the daily encountered optical and electronic devices constitute of transparent conductors. However, all the present available transparent conductors are n-type semiconductors, thus restricting technological advancement. The emergence of single-walled carbon nanotubes as p-type transparent conductors has been promising. Its further development will tremendously be instrumental for various opto-electronics and energy technologies. This work presents the development of state-of-the-art p-type transparent conductor using thin multicomponent layers and the introduction of carbon nanotube fibers. The newly developed conductor is certainly revolutionary for various single-walled carbon nanotubes application as shown in the fabricated hybrid heterojunction solar cells. This will open new avenues for its application in widespread technologies as in optoelectronics, photonics and energy.

Aalto-DD 79/2020

ISBN 978-952-60-3892-6 (printed)
ISBN 978-952-60-3893-3 (pdf)
ISSN 1799-4934 (printed)
ISSN 1799-4942 (pdf)

Aalto University
School of Science
Department of Applied Physics
www.aalto.fi

BUSINESS + ECONOMY

ART + DESIGN + ARCHITECTURE

SCIENCE + TECHNOLOGY

CROSSOVER

DOCTORAL DISSERTATIONS